

Discrete Cosserat Approach for Multisection Soft Manipulator Dynamics

Federico Renda ^{ID}, Member, IEEE, Frédéric Boyer, Member, IEEE, Jorge Dias ^{ID}, Member, IEEE, and Lakmal Seneviratne, Member, IEEE

Abstract—Nowadays, the most adopted model for the design and control of soft robots is the piecewise constant curvature model, with its consolidated benefits and drawbacks. In this work, an alternative model for multisection soft manipulator dynamics is presented based on a discrete Cosserat approach, in which the continuous Cosserat model is discretized by assuming a piecewise constant strain along the soft arm. As a consequence, the soft manipulator state is described by a finite set of constant strains. This approach has several advantages with respect to the existing models. First, it takes into account shear and torsional deformations, which are both essential to cope with out-of-plane external loads. Furthermore, it inherits desirable geometrical and mechanical properties of the continuous Cosserat model, such as intrinsic parameterization and greater generality. Finally, this approach allows to extend to soft manipulators, the recursive composite-rigid-body and articulated-body algorithms, whose performances are compared through a cantilever beam simulation. The soundness of the model is demonstrated through extensive simulation and experimental results.

Index Terms—Manipulator dynamics, robot kinematics, soft robotics.

NOMENCLATURE

0	Variable in the reference configuration.
\cdot	Derivative with respect to time.
$'$	Derivative with respect to space.
\wedge	Converts \mathbb{R}^6 in $\mathfrak{se}(3)$.
\sim	Converts \mathbb{R}^3 in $\mathfrak{so}(3)$.

Manuscript received March 20, 2018; revised July 9, 2018; accepted August 30, 2018. Date of publication October 19, 2018; date of current version December 4, 2018. This work was supported by the Faculty Start-up Award FSU-2018-08, Khalifa University Center for Autonomous Robotic System. This paper was recommended for publication by Associate Editor K. Xu and Editor P. Dupont upon evaluation of the reviewers' comments. (*Corresponding author: Federico Renda*)

F. Renda and L. Seneviratne are with the Mechanical Engineering Department, Khalifa University of Science and Technology, Abu Dhabi 127788, UAE, and also with KU-CARS, Khalifa University of Science and Technology, Abu Dhabi 127788, UAE (e-mail: federico.renda@ku.ac.ae; lakmal.seneviratne@ku.ac.ae).

F. Boyer is with the Department of Automatic Control, IMT Atlantique, Nantes, CS 20722 44307, France (e-mail: frederic.boyer@emn.fr).

J. Dias is with KU-CARS, Khalifa University of Science and Technology, Abu Dhabi 127788, UAE (e-mail: jorge@deec.uc.pt).

This paper has supplementary downloadable multimedia material available at <http://ieeexplore.ieee.org> provided by the authors. This includes a video simulation and experimental results of the discrete Cosserat model proposed in the manuscript. Multi-bending in-plane and out-of-plane motions have been taken into account. The model is validated against an octopus-inspired cable-driven manipulator. The algorithm used to solve such dynamic problems is described in the paper. This material is 6.89 MB in size.

Color versions of one or more of the figures in this paper are available online at <http://ieeexplore.ieee.org>.

Digital Object Identifier 10.1109/TRO.2018.2868815

t	$\in \mathbb{R}$ Time.
X	$\in [0, L] \subset \mathbb{R}$ Abscissa along the robot arm.
N	$\in \mathbb{N}$ Total number of sections.
g	$(X) = \begin{pmatrix} \mathbf{R} & \mathbf{u} \\ \mathbf{0}_T & 1 \end{pmatrix} \in SE(3)$ Configuration matrix.
Ad_g	$(X) = \begin{pmatrix} \mathbf{R} & \mathbf{0}_{3 \times 3} \\ \tilde{\mathbf{u}}\mathbf{R} & \mathbf{R} \end{pmatrix} \in \mathbb{R}^{6 \times 6}$ Adjoint representation of the configuration matrix.
Ad_g^*	$(X) = \begin{pmatrix} \mathbf{R} & \tilde{\mathbf{u}}\mathbf{R} \\ \mathbf{0}_{3 \times 3} & \mathbf{R} \end{pmatrix} \in \mathbb{R}^{6 \times 6}$ Coadjoint representation of the configuration matrix.
T_g	$(X) = \int_0^X \text{Ad}_{g(s)} ds \in \mathbb{R}^{6 \times 6}$ Tangent operator of the exponential map.
$\hat{\eta}$	$(X) = \begin{pmatrix} \mathbf{w} & \mathbf{v} \\ \mathbf{0}_T & 0 \end{pmatrix} \in \mathfrak{se}(3)$ Velocity twist vector.
$\hat{\xi}$	$(X) = \begin{pmatrix} \tilde{\mathbf{k}} & \mathbf{q} \\ \mathbf{0}_T & 0 \end{pmatrix} \in \mathfrak{se}(3)$ Strain twist vector.
$\text{ad}_{\xi, \eta}$	$(X) = \begin{pmatrix} \tilde{\mathbf{k}}, \tilde{\mathbf{w}} & \mathbf{0}_{3 \times 3} \\ \tilde{\mathbf{q}}, \tilde{\mathbf{v}} & \tilde{\mathbf{k}}, \tilde{\mathbf{w}} \end{pmatrix} \in \mathbb{R}^{6 \times 6}$ Adjoint representation of the strain twist vector.
$\text{ad}_{\xi, \eta}^*$	$(X) = \begin{pmatrix} \tilde{\mathbf{k}}, \tilde{\mathbf{w}} & \mathbf{0}_{3 \times 3} \\ \mathbf{0}_{3 \times 3}, \tilde{\mathbf{w}} & \tilde{\mathbf{k}}, \tilde{\mathbf{w}} \end{pmatrix} \in \mathbb{R}^{6 \times 6}$ Coadjoint representation of the strain twist vector.
\mathcal{T}	$(\eta) \in \mathbb{R}$ Reduced kinetics energy density.
\mathfrak{U}	$(\xi) \in \mathbb{R}$ Reduced elastic energy density.
\mathcal{F}_i	$(X) \in \mathbb{R}^6$ Wrench of internal force.
$\bar{\mathcal{F}}_a$	$(X) \in \mathbb{R}^6$ Distributed wrench of actuation loads.
$\bar{\mathcal{F}}_e$	$(X) \in \mathbb{R}^6$ Distributed wrench of external loads.
\mathcal{F}_p	$\in \mathbb{R}^6$ Wrench of external point loads.
\mathcal{J}	$(X) \in \mathbb{R}^{6 \times 6N}$ Soft robots <u>geometric Jacobian</u> .
S_i	$(X) \in \mathbb{R}^{6 \times 6}$ i^{th} 6×6 Component of the geometric Jacobian.
q	$= [\xi_1^T \ \xi_2^T \ \dots \ \xi_N^T]^T \in \mathbb{R}^{6N}$ Soft robots joint vector.
τ	$= [\tau_1^T \ \tau_2^T \ \dots \ \tau_N^T]^T \in \mathbb{R}^{6N}$ Soft robots elastic and actuation vector.
F	$(q) = [F_1^T \ F_2^T \ \dots \ F_N^T]^T \in \mathbb{R}^{6N}$ Generalized vector of external concentrated load.
M	$(q) \in \mathbb{R}^{6N \times 6N}$ Generalized inertia matrix.
C_1	$(q, \dot{q}) \in \mathbb{R}^{6N \times 6N}$ First Coriolis matrix.
C_2	$(q, \dot{q}) \in \mathbb{R}^{6N \times 6N}$ Second Coriolis matrix.
N	$(q) \in \mathbb{R}^{6N \times 6}$ Gravitational-buoyancy matrix.
D	$(q, \dot{q}) \in \mathbb{R}^{6N \times 6N}$ Drag matrix.

I. INTRODUCTION

SINCE the beginning of research in the field of soft robotics, many researchers have contributed in the development of mathematical modeling approaches that could be able to describe the kinematics and dynamics of such infinite degrees of freedom robots. However, addressing the requirements imposed by robotic applications is still a challenge [1], [2]. In order to

meet the standards achieved in traditional rigid robotics, a model for soft robotics should be, at the same time, computational inexpensive and sufficiently accurate. It should be able to shed light on the mathematical submodels, encompass them in a unified framework, and provide a systematic modeling procedure, regardless of the specific application. Such a modeling framework is the necessary condition for developing the physical designs and control architectures of these new soft robots as well as their task-related motions and path planning.

Although it may be tracked back to the pioneering works on flexible and compliant actuators [3], [4], the soft robotics field has a relative short history in its modern acceptance [5]. Despite this short time, important results have been achieved and several complementary modeling approaches have been proposed to date. In the following, we will focus on the group of continuous approaches, where our model falls into, while also discrete multibody approximations exist, such as [6], which are suitable when the manipulator cannot be reduced to a small number of sections.

A. State-of-the-Art Soft Manipulator Modeling

Among the continuous approaches, three main categories can be identified: piecewise constant curvature (PCC) models, continuous Cosserat models, and three-dimensional (3-D) finite element models (FEM).

The PCC modeling approach is by far the most adopted in the soft robotics community [7]. It represents the soft robot as a finite collection of circular arcs, which can be described by only three parameters (radius of curvature, angle of the arc, and bending plane), a simplification which drastically reduces the number of variables needed. Originally devoted to kinematics modeling [8], this approach has been extended and improved over the years with excellent results as in [9] and [10]. In spite of this success, the constant curvature assumption is not always valid, especially when the robot is subject to out-of-plane external loads, including gravity.

The continuous Cosserat approach is an infinite DoF model where the soft robot is represented by continuously stacking an infinite number of infinitesimal microsolids (for an exhaustive dissertation on the nonlinear theories of elasticity, including the Cosserat rod theory, see [11]). These microsolids can be two-dimensional, as the cross sections of a beam, or one-dimensional, as the rigid transverse fibers of a shell. In the robotics field, a precursory version of the Cosserat approach, consisting of a finite number of solids projected on a continuous backbone, has been applied to the dynamics of hyper-redundant robot in [12]. More recently, the Cosserat approach has been explicitly applied to soft robotics locomotion [13], [14] and manipulation [15], in both static [16] and dynamic [17] conditions. This approach has also been extended to continuum manipulators undergoing inflation [18] and to shell-like soft robots for underwater locomotion inspired by cephalopods [19], [20]. Despite their accuracy and fidelity to the continuum mechanics of the soft robots, the resulting partial differential equations are difficult to be used effectively for control purposes.

Finally, approaches based on 3-D FEM have also been explored for modeling and control of soft robots [21]. This ap-

proach has been so far limited to quasi-static conditions and requires a linearization of the geometric nonlinearity, which may result inefficient for very large displacements. Furthermore, a 3-D FEM approach does not provide geometric insights into the dynamic behavior of the manipulator.

B. Discrete Cosserat Approach

Although it might be impossible, due to physical reasons, to achieve the same standard possible when using mathematical models for rigid robotics, the research outlined above constitute a significant attempt in this direction. In the present paper, we build upon two of the main pillars achieved so far, the continuous Cosserat model and the piecewise constant curvature model. Going further into details, the PCC model, commonly used to reduce the dimension of the state space, is applied to discretize the continuous model developed with the Cosserat approach by assuming a piecewise constant deformation along the soft manipulator. As a consequence, the soft manipulator is completely described by a finite set of strain vectors, which plays the same role as that of the joint vector for traditional robotics.

The robot arm configuration is then reconstructed by means of the exponential map in SE(3), providing a direct forward kinematics between the joint space and the configuration space without any intermediate map. In contrast, the joint vector of the PCC model is represented by the actuation variables (usually actuator lengths), which need to be mapped into the arc parameters in order to construct the forward kinematics. For the same reason, the discrete Cosserat framework allows the implementation of different actuation solutions and external load models, including the interaction with a dense medium, without any significant changes in the structure of the model, and is so more independent from specific applications.

The strains allowed by the Cosserat approach include torsion and shears along with curvature and elongation. Thus, we call this method piecewise constant strain (PCS) model. With respect to the PCC model, the PCS model not only takes into account shears and torsion, which are both essential to cope with out-of-plane external loads, but also shares a common geometric structure with the equations of motion of their rigid robotics counterpart. As a matter of fact, being based on the SE(3) geometry of the Cosserat approach, the PCS model guarantees a better continuity with the rigid body geometry [again SE(3)] of traditional robotics.

In the authors' opinion, the distinctive features depicted above make of the proposed discrete Cosserat approach a promising attempt toward a unified mathematical framework between traditional and soft robotics.

C. Discrete Geometrically-Exact Approaches Comparison

The approach proposed shares many common points with the geometrically-exact FEM approach. However, all the FEMs of Cosserat beams are based on a parameterization of the motions with some position and orientation fields (transformation on a Lie group or quaternions) evaluated with respect to a fixed reference. This is the case of the geometrically exact FEM of Reissner beams [22], [23], [24], or that of Kirchhoff beams [25]. On the other hand, our approach is based on another

parameterization where the starting continuous fields are rather strain fields. This is a fundamental difference since in this case, the spatial discretization of the beam leads to some explicit integrals that can be performed analytically in a closed form as is done in this paper. In particular, in most of the approaches proposed so far, whether in the FEM mentioned above, as well as in the discrete geometrically-exact methods recently developed in [26], [27], and [28], the inextensibility and unshearability need to be addressed as constraints imposed to the position-orientation fields, while in our case, they can be explicitly tackled through the integration of the constrained strain twists.

The closest work to this here presented is due to Bertails [29]. In this reference, the author addresses the issue of the fast numerical simulation of unstretchable Kirchhoff rods for computational graphic applications. As in our case, the rod is parameterized with PCS fields (curvature and twist in this case). To perform fast dynamic simulations, the approach, named “Super-Helix” by her author, takes benefits from the strain parameterization to apply the recursive Featherstone algorithm of serial multibody systems [30]. As mentioned in [29], this super-helix approach is probably the most efficient proposed so far to address the challenging issues of the interactive manipulation of rods with knots, or the interactive simulation of hairs. In spite of these common foundations, the approach here proposed has been derived independently with different tools. In particular, the analytical exact calculation of the strain-parameterized fields is addressed in the wider context of SE(3), by using tools of geometric mechanics as the exponential map, which are today well spread in the robotics community [31]. This allows to capture all the internal beam kinematics as specific subcases, ranging from the simplest ones to the full Reissner kinematics where the six strain fields of a Cosserat beam are considered, including the case of unstretchable Kirchhoff rods. Moreover, the proposed framework provides several other models than the dynamic recursive model required by the Featherstone algorithm as the geometric model, the kinematic model (in the form of a geometric Jacobian), and the explicit Lagrangian model of these systems, which can greatly help researchers in developing soft robotic arms. In this perspective, the approach also pays a special attention to the crucial issue of actuation, which is irrelevant in the field of computational graphics.

D. Contribution With Respect to Previous Works and Outline

Part of the work shown here has been presented in a recently published conference paper [32], where the discrete Cosserat idea has been presented, for the first time, for a single section manipulator. An equivalent formulation has also been developed, although with a different approach, in [33], where the multisection kinematics is analyzed in depth. Beyond these works, the full multisection dynamics is addressed here for the general case of a soft manipulator operating in a dense medium like water. Furthermore, to solve the dynamic equation, two recursive algorithms, which extend the composite-rigid-body and articulated-body algorithms [30] to soft manipulators, are presented here and their performances are compared through benchmark simulation experiments. Finally, comprehensive

experimental results are shown using an octopus-inspired prototype.

In the following, in Section II, the continuous Cosserat model is briefly reminded in order to introduce the discretization developed in the subsequent Section III. In Section IV, the extension to soft manipulators of the recursive composite-rigid-body and articulated-body algorithms are presented and compared through a cantilever beam simulation. The model is finally corroborated through experimental results in Section V.

II. CONTINUOUS COSSERAT MODEL

In the Cosserat theory, the configuration of a microsolid of a soft body with respect to the spatial frame at a certain time is characterized by a position vector \mathbf{u} and an orientation matrix \mathbf{R} , parameterized by the material abscissa $X \in [0, L]$ along the robot arm. Thus, the configuration space is defined as a curve $\mathbf{g}(\cdot) : X \mapsto \mathbf{g}(X) \in \text{SE}(3)$ with

$$\mathbf{g} = \begin{pmatrix} \mathbf{R} & \mathbf{u} \\ \mathbf{0}^T & 1 \end{pmatrix}.$$

Then, the strain state of the soft arm is defined by the vector field along the curve $\mathbf{g}(\cdot)$ given by $X \mapsto \hat{\xi}(X) = \mathbf{g}^{-1} \partial \mathbf{g} / \partial X = \mathbf{g}^{-1} \mathbf{g}' \in \mathfrak{se}(3)$, where the hat is the isomorphism between the twist vector representation and the matrix representation of the Lie algebra $\mathfrak{se}(3)$. The components of this field are specified in the (micro)body frames as

$$\hat{\xi} = \begin{pmatrix} \tilde{\mathbf{k}} & \mathbf{q} \\ \mathbf{0}^T & 0 \end{pmatrix} \in \mathfrak{se}(3), \quad \xi = (\mathbf{k}^T, \mathbf{q}^T)^T \in \mathbb{R}^6$$

where $\mathbf{q}(X)$ represents the linear strains, and $\mathbf{k}(X)$ the angular strains. The tilde is the isomorphism between 3-D vectors and skew symmetric matrices.

The time evolution of the configuration curve $\mathbf{g}(\cdot)$ is represented by the twist vector field $X \mapsto \eta(X) \in \mathbb{R}^6$ defined by $\hat{\eta}(X) = \mathbf{g}^{-1} \partial \mathbf{g} / \partial t = \mathbf{g}^{-1} \dot{\mathbf{g}}$. This field can be detailed in terms of its components in the (micro)body frames as

$$\hat{\eta} = \begin{pmatrix} \tilde{\mathbf{w}} & \mathbf{v} \\ \mathbf{0}^T & 0 \end{pmatrix} \in \mathfrak{se}(3), \quad \eta = (\mathbf{w}^T, \mathbf{v}^T)^T \in \mathbb{R}^6$$

where $\mathbf{v}(X)$ and $\mathbf{w}(X)$ are respectively the linear and angular velocity at a given time instant.

A. Continuous Kinematics

Given the above construction, we can obtain the kinematic equations relating the strains of the robot arm ξ with the position \mathbf{g} , velocity η , and acceleration $\dot{\eta}$ for each infinitesimal microsolid constituting the robot. By definition, the first equation is given by

$$\mathbf{g}' = \mathbf{g}\hat{\xi}. \quad (1)$$

Then, the equality of mixed partial derivatives $(\dot{\mathbf{g}})' = (\dot{\mathbf{g}}')$ gives the following compatibility equation between strain and velocity:

$$\eta' = \dot{\xi} - \text{ad}_{\xi} \eta \quad (2)$$

where ad is the adjoint map defined in Appendix A together with the coadjoint map ad^* .

Finally, by taking the derivative of (2) with respect to time, we obtain the continuous model of acceleration

$$\ddot{\eta}' = \ddot{\xi} - \text{ad}_{\dot{\xi}}\eta - \text{ad}_{\dot{\xi}}\dot{\eta}. \quad (3)$$

B. Continuous Dynamics

In [34], it is shown that Cosserat beam dynamics can be directly derived from the extension to continuum media of a variational calculus originally introduced by Poincaré [35]. In contrast to the usual Lagrangian mechanics, this calculus allows deriving the dynamics of a system whose configuration space definition requires the structure of Lie group. In this context, the dynamics of the Cosserat medium can be entirely derived from a Lagrangian density $\mathcal{T}(\eta) - \mathfrak{U}(\xi)$, where \mathcal{T} and \mathfrak{U} are functions of the Lie algebra vectors modeling the densities of kinetic and elastic energy of the Cosserat beam per unit of material length X . Applying this variational calculus to such a density leads to the strong form of a Cosserat beam with respect to the microsolid frames

$$\mathcal{M}\dot{\eta} + \text{ad}_\eta^*\mathcal{M}\eta = \mathcal{F}'_i + \text{ad}_\xi^*\mathcal{F}_i + \bar{\mathcal{F}}_a + \bar{\mathcal{F}}_e \quad (4)$$

where $\mathcal{F}_i(X) = \partial\mathfrak{U}/\partial X$ is the wrench of internal forces, $\bar{\mathcal{F}}_a(X, t)$ is the distributed actuation loads, $\bar{\mathcal{F}}_e(X)$ is the external wrench of distributed applied forces, and $\mathcal{M}(X)$ is the screw inertia matrix. Let us specify the angular and linear components of the internal and external wrenches: $\mathcal{F}_i = (\mathbf{M}_i^T, \mathbf{N}_i^T)^T$, $\bar{\mathcal{F}}_a = (\mathbf{m}_a^T, \mathbf{n}_a^T)^T$, $\bar{\mathcal{F}}_e = (\mathbf{m}_e^T, \mathbf{n}_e^T)^T \in \mathbb{R}^6$, where $\mathbf{N}_i(X)$ and $\mathbf{M}_i(X)$ are the internal force and torque vectors, $\mathbf{n}_a(X, t)$ and $\mathbf{m}_a(X, t)$ are the distributed actuation force and torque inputs, while $\mathbf{n}_e(X)$ and $\mathbf{m}_e(X)$ are the distributed external force and torque for unit of X . By choosing a local (micro)body frame oriented as in Fig. 2, with the X axis pointing toward the tip of the robot arm, and the Y and Z axes lying on the plane of the section (considered symmetric), the screw inertia matrix can be written as: $\mathcal{M} = \text{diag}(J_x, J_y, J_z, A, A, A)\rho$, where ρ is the body density, A is the section area, and J_y , J_z , and J_x are, respectively, the bending and torsion second moment of inertia of the beam cross-section.

Let us now specify the models of the distributed actuation, external load, and internal forces appearing in (4) for the general case of a soft robot arm moving in a dense surrounding medium like water.

We consider here a cable-driven actuation mechanism (see [36] and [37]), even though the proposed approach is not limited to a specific actuation model. For cable-driven actuation, we have (see [15] and [17])

$$\bar{\mathcal{F}}_a(X, t) = -(\mathcal{F}'_a + \text{ad}_\xi^*\mathcal{F}_a) \quad (5)$$

where $\mathcal{F}_a(X, t) \in \mathbb{R}^6$ is the point load generated by a cable at any arbitrary microsolid, expressed in (micro)body coordinate. The value of \mathcal{F}_a depends on the cable path inside the robot arm. Let's define $\mathbf{g}_c(X) \in \text{SE}(3)$, the position and orientation of the cable with respect to the midline of the arm (see Fig. 1). Then, the cable's point load is given by $\mathcal{F}_a = \text{Ad}_{\mathbf{g}_c}^*[0 \ 0 \ 0 \ -T \ 0 \ 0]^T$,

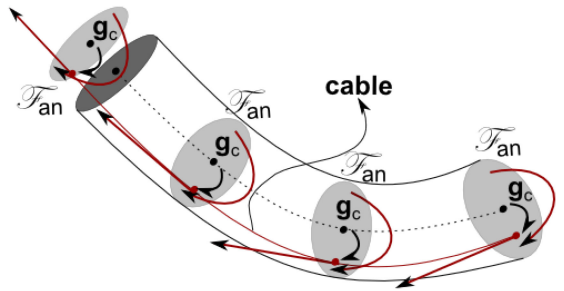


Fig. 1. Schematic of the cable-driven actuation for one section.

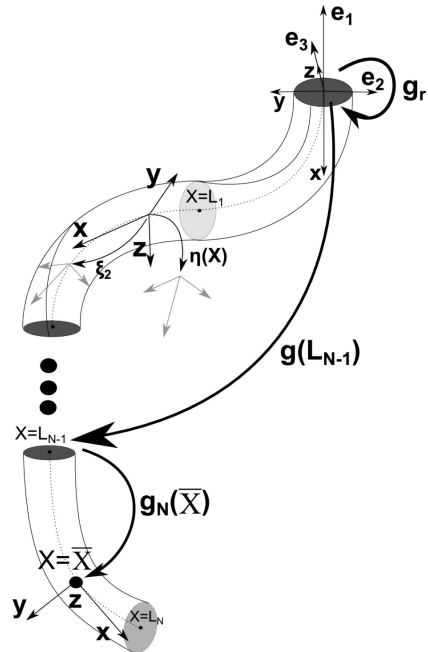


Fig. 2. Schematic of the kinematics of the piecewise constant strain model.

where $T(t) \in \mathbb{R}^+$ is the tension of the cable and we have defined the adjoint representation (Ad) of the Lie group SE(3) (see Nomenclature). For example, if a cable is parallel to the midline at a distance d from the center, we obtain a constant load $\mathcal{F}_a = [0 \ -Td \ 0 \ -T \ 0 \ 0]^T$, where we have supposed the cable to pass across the local positive z axis.

Regarding the wrench of internal passive forces, a linear viscoelastic constitutive model, based on the Kelvin–Voigt assumptions, is chosen [17]

$$\mathcal{F}_i(X) = \Sigma(\xi - \xi^0) + \Upsilon\dot{\xi} \quad (6)$$

where Σ and Υ are constant screw stiffness and viscosity matrices, equal to $\Sigma = \text{diag}(GJ_x, EJ_y, EJ_z, EA, GA, GA)$, $\Upsilon = \text{diag}(J_x, 3J_y, 3J_z, 3A, A, A)v$, E being the Young modulus, G the shear modulus, and v the shear viscosity modulus; $\xi^0 = [0 \ 0 \ 0 \ 1 \ 0 \ 0]^T$ stands for the zeros strain vector in the reference straight configuration. No other assumptions, except the constitutive model, are needed to describe the elastic behavior of the robot arm.

As for the external loads, we have considered the general case of underwater operation, i.e., distributed loads due to gravity and

buoyancy, drag, added mass, and a concentrated/point load due to externally applied loads or contacts [17]

$$\begin{aligned}\bar{\mathcal{F}}_e &= (1 - \rho_w / \rho) \mathcal{M} \text{Ad}_{\mathbf{g}_r \mathbf{g}(X)}^{-1} \mathcal{G} - \mathcal{D} \|\mathbf{v}\| \boldsymbol{\eta} + \delta(X - \bar{X}) \mathcal{F}_p \\ \mathcal{M}_a &= \mathcal{M} + \mathcal{A}\end{aligned}\quad (7)$$

where ρ_w is the water density, $\mathcal{G} = [0 \ 0 \ 0 \ -9.81 \ 0 \ 0]^T$ is the gravity twist with respect to the spatial frame (in accordance with the choice of the spatial frame (e_1, e_2, e_3) given in Fig. 2), \mathbf{g}_r is the transformation between the spatial frame and the base frame of the soft manipulator, $\mathcal{D}(X)$ is the screw matrix of the drag fluid dynamics coefficient, $\delta(\cdot)$ is the Dirac distribution, \mathcal{F}_p is the wrench corresponding to the point load applied at \bar{X} , and $\mathcal{A}(X)$ is the screw matrix of the added mass fluid dynamics coefficient. Note here that replacing \mathcal{M} by \mathcal{M}_a in (4) allows modeling inertial hydrodynamics forces exerted along the arm. Finally, when the soft arm is working in a sparse medium like air, we will let ρ_w , and consequently \mathcal{D} and \mathcal{A} , be equal to zero.

III. DISCRETE COSSERAT MODEL

Equations (1)–(4) of the continuous Cosserat model are suitable to model the kinematics and dynamics of soft robots expressing a nonconstant deformation, as it has been presented in [17]. In the subsequent development, we unify the constant and nonconstant cases under the same mathematical framework. To that end, the continuous model is discretized by an analytic spatial integration. This is allowed by the PCS assumption which provides the condition to analytically integrate the continuous model and leads to the extension of the piecewise constant curvature model, by including torsion and shears, without any additional effort. Furthermore, a profound and useful parallelism with the rigid manipulators theory can be achieved, which leads to the soft robot counterpart of the Lagrangian model of rigid serial manipulators.

A. PCS Kinematics

At any instant t , considering the strain field ξ constant along each of the N sections of the soft arm, we can replace the continuous field with a finite set of N twist vectors ξ_n ($n \in \{1, 2, \dots, N\}$), which play the role of the joint variables of traditional rigid robotics. Under this assumption, (1) becomes a homogeneous, linear, matrix differential equation with constant coefficients, which can be analytically solved at any section n using the matrix exponential method with the appropriate interval of X and initial value [38]. Going further into details, the material abscissa $X \in [0, L]$ is divided into N sections of the form $[0, L_1], [L_1, L_2] \dots [L_{N-1}, L_N]$ (with $L_N = L$) and the initial value for the differential equation of the section n is given by the solution at the right boundary of the previous section ($X = L_{n-1}$). In other words, the solutions are glued together, one on top of the other. With these considerations, the integration of (1) at a certain instant t becomes

$$\mathbf{g}(X) = \mathbf{g}(L_{n-1}) e^{(X-L_{n-1})\hat{\xi}_n}. \quad (8)$$

It turns out that the infinite series of the exponential in (8) can be expressed in a compact way as follows [39]:

$$\begin{aligned}e^{(X-L_{n-1})\hat{\xi}_n} &= \mathbf{I}_4 + (X - L_{n-1}) \hat{\xi}_n \\ &+ \frac{1}{\theta_n^2} (1 - \cos((X - L_{n-1}) \theta_n)) \hat{\xi}_n^2 \\ &+ \frac{1}{\theta_n^3} ((X - L_{n-1}) \theta_n - \sin((X - L_{n-1}) \theta_n)) \hat{\xi}_n^3 =: g_n(X)\end{aligned}\quad (9)$$

where $\theta_n^2 = \mathbf{k}_n^T \mathbf{k}_n$. For straight configurations of the section, we have $\mathbf{k}_n = \mathbf{0}$ and consequently $\hat{\xi}_n^2 = \mathbf{0}_{4 \times 4}$. In this case, (9) becomes [39]

$$e^{(X-L_{n-1})\hat{\xi}_n} = \mathbf{I}_4 + (X - L_{n-1}) \hat{\xi}_n$$

which allows circumventing the well-known singularity of straight arm pose of the PCC models [40], [41]. Equation (9) can be viewed as the SE(3) counterpart of the Rodrigues formula for SO(3). Calling $\mathbf{g}_n(X)$ the exponential function in (8) and (9) can be written in the more familiar way

$$\mathbf{g}(X) = \mathbf{g}(L_{n-1}) \mathbf{g}_n(X) \quad (10)$$

which recursively returns the position and orientation of the microsolid at X knowing the set of strains ξ_n only.

Similarly, the velocity of each microsolid $\boldsymbol{\eta}(X)$ can be obtained by a piecewise integration of the continuous model (2). Under constant strain condition, at each section n and time t , (2) is a nonhomogeneous, linear, matrix differential equation with constant coefficients (recall that ξ_n is also piecewise constant) which can be analytically solved using the variation of parameters method, with the appropriate initial value [38]

$$\begin{aligned}\boldsymbol{\eta}(X) &= e^{-(X-L_{n-1})\text{ad}_{\xi_n}} \\ &\left(\boldsymbol{\eta}(L_{n-1}) + \int_{L_{n-1}}^X e^{(s-L_{n-1})\text{ad}_{\xi_n}} ds \dot{\xi}_n \right).\end{aligned}\quad (11)$$

Again, the exponential function in (11) can be expressed with a finite number of terms [39] (for the sake of presentation, $x = X - L_{n-1}$ holds in the following)

$$\begin{aligned}e^{x\text{ad}_{\xi_n}} &= \mathbf{I}_6 + \frac{1}{2\theta_n} (3 \sin(x\theta_n) - x\theta_n \cos(x\theta_n)) \text{ad}_{\xi_n} \\ &+ \frac{1}{2\theta_n^2} (4 - 4 \cos(x\theta_n) - x\theta_n \sin(x\theta_n)) \text{ad}_{\xi_n}^2 \\ &+ \frac{1}{2\theta_n^3} (\sin(x\theta_n) - x\theta_n \cos(x\theta_n)) \text{ad}_{\xi_n}^3 \\ &+ \frac{1}{2\theta_n^4} (2 - 2 \cos(x\theta_n) - x\theta_n \sin(x\theta_n)) \text{ad}_{\xi_n}^4 \\ &= \text{Ad}_{\mathbf{g}_n(X)}\end{aligned}\quad (12)$$

where for straight configurations we have $\text{ad}_{\xi_n}^2 = \mathbf{0}_{6 \times 6}$ and thus, taking the limit for $\theta_n \rightarrow 0$, $e^{x\text{ad}_{\xi_n}} = \mathbf{I}_6 + x\text{ad}_{\xi_n}$. Thanks to the fact that $e^{\text{ad}_{\xi}} = \text{Ad}_{\tilde{\xi}}$ [42, p. 403, Lemma 7.5.9], we can notice that the exponential function (12) is nothing else, but the adjoint representation of the Lie group transformation $\mathbf{g}_n(X)$

of (9). With this definition at hand, (11) can be rewritten as follows:

$$\boldsymbol{\eta}(X) = \text{Ad}_{\mathbf{g}_n(X)}^{-1} \left(\boldsymbol{\eta}(L_{n-1}) + \text{T}_{\mathbf{g}_n(X)} \dot{\boldsymbol{\xi}}_n \right) \quad (13)$$

where we have defined the tangent operator of the exponential map [23]

$$\begin{aligned} \text{T}_{\mathbf{g}_n(X)} &:= \int_{L_{n-1}}^X \text{Ad}_{\mathbf{g}_n(s)} ds \\ &= x \mathbf{I}_6 + \frac{1}{2\theta_n^2} (4 - 4 \cos(x\theta_n) - x\theta_n \sin(x\theta_n)) \text{ad}_{\boldsymbol{\xi}_n} \\ &\quad + \frac{1}{2\theta_n^3} (4x\theta_n - 5 \sin(x\theta_n) + x\theta_n \cos(x\theta_n)) \text{ad}_{\boldsymbol{\xi}_n}^2 \\ &\quad + \frac{1}{2\theta_n^4} (2 - 2 \cos(x\theta_n) - x\theta_n \sin(x\theta_n)) \text{ad}_{\boldsymbol{\xi}_n}^3 \\ &\quad + \frac{1}{2\theta_n^5} (2x\theta_n - 3 \sin(x\theta_n) + x\theta_n \cos(x\theta_n)) \text{ad}_{\boldsymbol{\xi}_n}^4. \end{aligned} \quad (14)$$

Remarkably, (13) recursively computes the velocity of any micro-solid at X along the soft arm as a function of the set of strains $\boldsymbol{\xi}_n$ and strain rates $\dot{\boldsymbol{\xi}}_n$.

Finally, the acceleration of any microsolid at X ($\ddot{\boldsymbol{\eta}}(X)$) can be calculated at any time t , by means of a piecewise integration of the continuous (3). Considering constant strains along one section, (3) is again a nonhomogeneous, linear, matrix differential equation with constant coefficients. A direct application of the variation of parameters method with the appropriate initial value gives

$$\begin{aligned} \ddot{\boldsymbol{\eta}}(X) &= e^{-x \text{ad}_{\boldsymbol{\xi}_n}} \\ &\quad \left(\ddot{\boldsymbol{\eta}}(L_{n-1}) + \int_{L_{n-1}}^X e^{x \text{ad}_{\boldsymbol{\xi}_n}} \left(\ddot{\boldsymbol{\xi}}_n - \text{ad}_{\dot{\boldsymbol{\xi}}_n} \boldsymbol{\eta} \right) ds \right). \end{aligned} \quad (15)$$

Then, by virtue of the definitions of $\text{Ad}_{\mathbf{g}_n}$, $\text{T}_{\mathbf{g}_n}$, we obtain

$$\begin{aligned} \ddot{\boldsymbol{\eta}}(X) &= \text{Ad}_{\mathbf{g}_n(X)}^{-1} \\ &\quad \left(\ddot{\boldsymbol{\eta}}(L_{n-1}) + \text{T}_{\mathbf{g}_n(X)} \ddot{\boldsymbol{\xi}}_n - \int_{L_{n-1}}^X \text{Ad}_{\mathbf{g}_n(s)} \text{ad}_{\dot{\boldsymbol{\xi}}_n} \boldsymbol{\eta}(s) ds \right). \end{aligned} \quad (16)$$

Let us focus on the term $\text{Ad}_{\mathbf{g}_n(s)} \text{ad}_{\dot{\boldsymbol{\xi}}_n} \boldsymbol{\eta}(s)$ inside the integral of the right-end side. First, by means of (13) and the properties

$$\boldsymbol{J}(X) = \begin{cases} \left[(\text{Ad}_{\mathbf{g}_1}^{-1} \text{T}_{\mathbf{g}_1})(X) \ 0_6 \ \cdots \right] & \text{if } 0 < X \leq L_1 \\ \left[\text{Ad}_{\mathbf{g}_2(X)}^{-1} (\text{Ad}_{\mathbf{g}_1}^{-1} \text{T}_{\mathbf{g}_1})(L_1) \ (\text{Ad}_{\mathbf{g}_2}^{-1} \text{T}_{\mathbf{g}_2})(X) \ 0_6 \ \cdots \right] & \text{if } L_1 < X \leq L_2 \\ \left[\text{Ad}_{\mathbf{g}_3(X)}^{-1} \text{Ad}_{\mathbf{g}_2(L_2)}^{-1} (\text{Ad}_{\mathbf{g}_1}^{-1} \text{T}_{\mathbf{g}_1})(L_1) \ \text{Ad}_{\mathbf{g}_3(X)}^{-1} (\text{Ad}_{\mathbf{g}_2}^{-1} \text{T}_{\mathbf{g}_2})(L_2) \ \cdots \ 0_6 \right] & \text{if } L_1 < X \leq L_2 \\ \vdots & \vdots \\ \left[\prod_{j=1}^{N-1} \text{Ad}_{\mathbf{g}_j(\min(L_j, X))}^{-1} \text{T}_{\mathbf{g}_1(L_1)} \ \cdots \ (\text{Ad}_{\mathbf{g}_N}^{-1} \text{T}_{\mathbf{g}_N})(X) \right] & \text{if } L_{N-1} < X \leq L_N \end{cases} \quad (20)$$

of the adjoint map, we have

$$\text{Ad}_{\mathbf{g}_n(s)} \text{ad}_{\dot{\boldsymbol{\xi}}_n} \boldsymbol{\eta}(s) = \text{ad}_{\text{Ad}_{\mathbf{g}_n(s)} \dot{\boldsymbol{\xi}}_n} \left(\boldsymbol{\eta}(L_{n-1}) + \text{T}_{\mathbf{g}_n(s)} \dot{\boldsymbol{\xi}}_n \right).$$

Then, evoking the linearity and anticommutativity of the adjoint map, and using (12) and (14), we obtain the equivalence

$$\text{Ad}_{\mathbf{g}_n(s)} \text{ad}_{\dot{\boldsymbol{\xi}}_n} \boldsymbol{\eta}(s) = \text{ad}_{\text{Ad}_{\mathbf{g}_n(s)} \dot{\boldsymbol{\xi}}_n} \boldsymbol{\eta}(L_{n-1})$$

which once substituted in (16) (and using the anticommutativity of the adjoint map to make appear $\text{T}_{\mathbf{g}_n}$), gives the model of accelerations as follows:

$$\ddot{\boldsymbol{\eta}}(X) = \text{Ad}_{\mathbf{g}_n}^{-1} \left(\ddot{\boldsymbol{\eta}}(L_{n-1}) + \text{ad}_{\boldsymbol{\eta}(L_{n-1})} \text{T}_{\mathbf{g}_n} \dot{\boldsymbol{\xi}}_n + \text{T}_{\mathbf{g}_n} \ddot{\boldsymbol{\xi}}_n \right). \quad (17)$$

Again, (17) returns the acceleration of any microsolid at X by means of the set of strains $\boldsymbol{\xi}_n$, strain rates $\dot{\boldsymbol{\xi}}_n$, and rates of strain rate $\ddot{\boldsymbol{\xi}}_n$ only.

1) Geometric Jacobian: In order to develop the discrete Cosserat dynamic model for soft robots, a relation between the kinematics quantities $\boldsymbol{\eta}$, $\dot{\boldsymbol{\eta}}$ and a joint vector for soft robotics needs to be established. To do so, we backtrack to the base the velocity term $\boldsymbol{\eta}(L_{n-1})$ on the right-end side of (13), which becomes

$$\boldsymbol{\eta}(X) = \sum_{i=1}^n \text{Ad}_{\mathbf{g}_i(L_i) \cdots \mathbf{g}_n(X)}^{-1} \text{T}_{\mathbf{g}_i(\min(L_i, X))} \dot{\boldsymbol{\xi}}_i \quad (18)$$

where j is a descending index, we have considered a fixed base ($\boldsymbol{\eta}(0) = \mathbf{0}_{6 \times 1}$) and $L_{n-1} < X \leq L_n$. Introducing the soft robots joint vector

$$\boldsymbol{q} = [\boldsymbol{\xi}_1^T \ \boldsymbol{\xi}_2^T \ \cdots \ \boldsymbol{\xi}_N^T]^T \in \mathbb{R}^{6N}$$

(18) can be expressed as:

$$\boldsymbol{\eta}(X) = \boldsymbol{J}(X) \dot{\boldsymbol{q}} \quad (19)$$

which define the soft robots geometric Jacobian $\boldsymbol{J}(X) \in \mathbb{R}^{6 \times 6N}$ shown in (20) shown at the bottom of this page.

It is important to notice that the Jacobian (20) is calculated directly from the strains $\boldsymbol{\xi}_n$ by means of (12) and (14). For this reason, in accordance with the rigid manipulators theory, it is referred to as geometric Jacobian, in contrast with the analytic Jacobian. Furthermore, the action of the Jacobian $\boldsymbol{J}(X)$ on the joint vector \boldsymbol{q} returns the body velocity $\boldsymbol{\eta}(X)$ which is expressed in the (micro)body coordinate frame. Accordingly, $\boldsymbol{J}(X)$ is called body Jacobian.

Finally, by taking the time derivative of (19), the acceleration vector $\dot{\eta}(X)$ is obtained as

$$\dot{\eta}(X) = \mathbf{J}(X)\ddot{q} + \dot{\mathbf{J}}(X)\dot{q} \quad (21)$$

where $\dot{\mathbf{J}}(X)$ is obtained by a lengthy but straightforward calculation. Defining the 6×6 components of the Jacobian as $\mathbf{J}(X) = [S_1(X) \ S_2(X) \ \dots \ S_N(X)]$, the time derivative of the Jacobian can be expressed as

$$\dot{\mathbf{J}}(X) = -\sum_{i=1}^{n-1} \text{ad}_{\sum_{j=i+1}^n S_j(X)\dot{\xi}_j} \mathbf{J}_i(X) \quad (22)$$

where $L_{n-1} < X \leq L_n$ and we have defined $\mathbf{J}_i(X)$ as the Jacobian containing $\mathbf{0}_{6 \times 6}$ elements except for the i th: $\mathbf{J}_i(X) := [\mathbf{0}_{6 \times 6} \ \dots \ S_i(X) \ \dots \ \mathbf{0}_{6 \times 6}] \in \mathbb{R}^{6 \times 6N}$. Alternatively, (21) and the expression of Jacobian derivative (22) can be obtained by backtracking the acceleration $\dot{\eta}(L_{n-1})$ and velocity $\eta(L_{n-1})$ terms on the right side of (17).

2) Comparison With the PCC Model: The development above led us to three kinematics (8), (19), and (21), which give a model to calculate all the kinematic quantities from the knowledge of the joint space of the piecewise soft arm, in a very similar fashion to traditional rigid manipulators.

Compared to the PCC model, the discrete Cosserat approach presented here is able to handle not only constant curvature and elongation, but also shear and torsion, which are fundamental to deal with the strong interactions with the environment characteristic of locomotion and manipulation. Furthermore, the joint space \mathbf{q} composed by the N constant strains ξ_n represents an intrinsic parameterization and is directly mapped to the configuration space through the forward kinematics (8), (19), and (21). In the PCC model, instead, an additional intermediate step is needed, where the joint space (composed usually by the length of the actuators) is mapped to the arc parameter space (composed by the length, the curvature, and the plane of bending of the section). This has allowed us to build a geometric Jacobian instead of an analytic Jacobian, which preserves the natural geometric structure of the motion.

B. Piecewise Constant Strain Dynamics

In this section we derive the generalized equation of motion of the multisection PCS model. To that end, we reconsider the continuous dynamics (4), that we restate in the weak form of virtual works, i.e., for any field: $\delta\zeta(\cdot) : X \mapsto \delta\zeta(X) \in \mathbb{R}^6$

$$\begin{aligned} \int_0^L \delta\zeta^T (\mathcal{M}\dot{\eta} + \text{ad}_{\eta}^* \mathcal{M}\eta - \mathcal{F}'_i - \text{ad}_{\xi}^* \mathcal{F}_i - \bar{\mathcal{F}}_a - \bar{\mathcal{F}}_e) dX \\ = 0. \end{aligned} \quad (23)$$

Note that the above-mentioned weak form can be derived from the extended Poincaré variational calculus of [43]. Though being equivalent to the strong form (4), this weak form has the advantage of being directly usable to shift the dynamics from the continuous to our piecewise discrete approach. In fact, to derive the discrete dynamics corresponding to the discrete kinematics (10), it suffices to introduce the relation: $\delta\zeta(X) = \mathbf{J}(X)\delta q$ in addition to the kinematics relations (19) and (21). In these

conditions, (23) becomes

$$\begin{aligned} \forall \delta q \in \mathbb{R}^{6N} : \\ \delta q^T \int_0^L \mathbf{J}^T [\mathcal{M}(\mathbf{J}\ddot{q} + \dot{\mathbf{J}}\dot{q}) + \text{ad}_{\mathbf{J}\dot{q}}^* (\mathcal{M}\mathbf{J}\dot{q})] \\ - \mathbf{J}^T (\mathcal{F}'_i + \text{ad}_{\xi}^* \mathcal{F}_i + \bar{\mathcal{F}}_a + \bar{\mathcal{F}}_e) dX = 0 \end{aligned} \quad (24)$$

which leads to the following generalized dynamics equation once the external loads (7) and cable-driven actuation (5) are introduced in (24)

$$\begin{aligned} \left[\int_0^{L_N} \mathbf{J}^T \mathcal{M}_a \mathbf{J} dX \right] \ddot{q} + \left[\int_0^{L_N} \mathbf{J}^T \text{ad}_{\mathbf{J}\dot{q}}^* \mathcal{M}_a \mathbf{J} dX \right] \dot{q} \\ + \left[\int_0^{L_N} \mathbf{J}^T \mathcal{M}_a \dot{\mathbf{J}} dX \right] \dot{q} = \\ \int_0^{L_N} \mathbf{J}^T (\mathcal{F}'_i - \mathcal{F}'_a + \text{ad}_{\xi_n}^* (\mathcal{F}_i - \mathcal{F}_a)) dX + \mathbf{J}(\bar{X})^T \mathcal{F}_p \\ + (1 - \rho_w/\rho) \left[\int_0^{L_N} \mathbf{J}^T \mathcal{M} \text{Ad}_{\mathbf{g}}^{-1} dX \right] \text{Ad}_{\mathbf{g}_r}^{-1} \mathcal{G} \\ - \left[\int_0^{L_N} \mathbf{J}^T \mathcal{D} \mathbf{J} |\mathbf{J}\dot{q}|_v dX \right] \dot{q}. \end{aligned} \quad (25)$$

In (25), when needed, n represents the section corresponding to the running value of X inside the integrals and $|\cdot|_v$ takes the norm of the translational part of the operand, according to (7).

Finally, by defining each term and naming the coefficients matrices in squared parenthesis of (25), we obtain the PCS dynamic equation

$$\begin{aligned} \mathbf{M}(\mathbf{q})\ddot{q} + (\mathbf{C}_1(\mathbf{q}, \dot{q}) + \mathbf{C}_2(\mathbf{q}, \dot{q}))\dot{q} \\ = \boldsymbol{\tau}(\mathbf{q}) + \mathbf{F}(\mathbf{q}) + \mathbf{N}(\mathbf{q}) \text{Ad}_{\mathbf{g}_r}^{-1} \mathcal{G} - \mathbf{D}(\mathbf{q}, \dot{q})\dot{q} \end{aligned} \quad (26)$$

where we recognize the structure of the Lagrangian model of rigid serial manipulators.

In the remaining part of the section, we will describe the different components of (26).

1) Internal Elastic and Actuation Load: Let us start with the internal elastic and actuation load [the term with \mathcal{F}_i and \mathcal{F}_a in (25)], defined as

$$\boldsymbol{\tau} = [\boldsymbol{\tau}_1^T \ \boldsymbol{\tau}_2^T \ \dots \ \boldsymbol{\tau}_N^T]^T \in \mathbb{R}^{6N}.$$

Due to the linearity of the integral, each element $\boldsymbol{\tau}_n$ has the form

$$\boldsymbol{\tau}_n = \sum_{j=n}^N \int_{L_{j-1}}^{L_j} \mathbf{S}_n^T (\mathcal{F}'_i - \mathcal{F}'_a + \text{ad}_{\xi_n}^* (\mathcal{F}_i - \mathcal{F}_a)) dX$$

where we note that by definition $\mathbf{S}_n(X) = \mathbf{0}_{6 \times 6}$ for $X \leq L_{n-1}$ (see Fig. 3). Each of the integrals in the series, except of the first, can be directly solved analytically making use of the identity $\text{Ad}_{\mathbf{g}}^* (\mathcal{F}' + \text{ad}_{\xi} \mathcal{F}) = (\text{Ad}_{\mathbf{g}}^* \mathcal{F})'$, while the first one can be analytically solved with an integration by part with the additional use of the identity $\mathbf{T}_g^{T'} = \text{Ad}_g^T = \text{Ad}_{g^{-1}}^*$. Applying this operation, we obtain the internal elastic and actuation load for

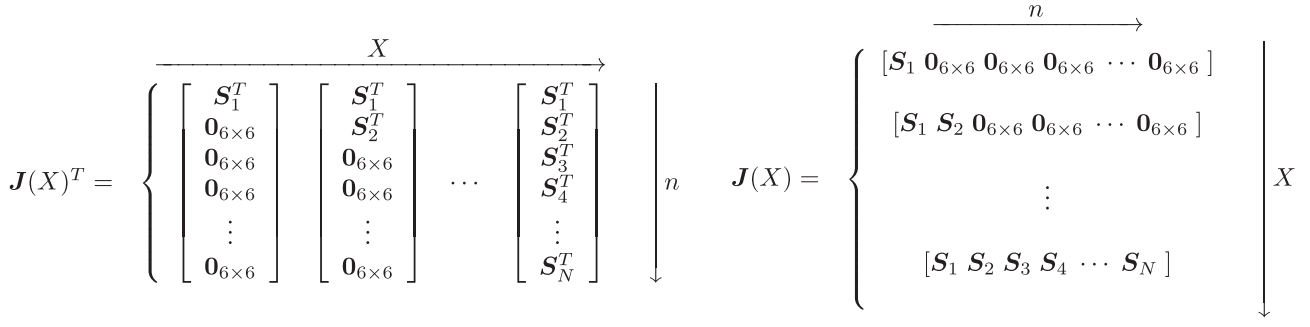


Fig. 3. Schematic of the Jacobian and its transposed highlighting the structure with respect to the position X and section n .

the section n as follows:

$$\boldsymbol{\tau}_n = \sum_{j=n}^N (\mathbf{S}_n^T (\mathcal{F}_i - \mathcal{F}_a))|_{L_{j-1}}^{L_j} - l(\mathcal{F}_i - \mathcal{F}_a) \quad (27)$$

where l is the length of the section equal to $L_n - L_{n-1}$ and we have assumed elastic and actuation load constant along the section, i.e., $\mathcal{F}_a(L_{n-1} < X < L_n) = \mathcal{F}_a$ and $\mathcal{F}_i(L_{n-1} < X < L_n) = \mathcal{F}_i$ are constants. It is worth to remark that we have not introduced any limitation on the kind of constitutive law governing the internal elastic force \mathcal{F}_i . Here a linear viscoelastic constitutive law is chosen (6), however, any nonlinear relation could be similarly adopted, while the present exposition would remain unchanged.

In order to calculate the sum in (27), we exploit the boundary condition at each section. For cable-driven actuation, they are given by

$$\begin{aligned} \mathcal{F}_i(L_n^+) &= \mathcal{F}_{i(n+1)} \mathcal{F}_i(L_n^-) = \mathcal{F}_{i(n+1)} + \mathcal{F}_{\text{an}} \\ \mathcal{F}_a(L_n^+) &= \sum_{j=n+1}^N \mathcal{F}_{aj} \mathcal{F}_a(L_n^-) = \sum_{j=n}^N \mathcal{F}_{aj} \end{aligned} \quad (28)$$

where the cables are assumed to run from the point of anchorage to the base of the manipulator. The contribution of the cables attached at L_n is indicated with \mathcal{F}_{an} (see Fig. 1) and the constant internal load of the section n with \mathcal{F}_{in} . As expected, crossing an anchoring edge L_n causes a jump in both the internal elastic and actuation load due respectively to the concentrated load of the cables anchored at that position and the sudden increase of the number of cable running through the section. Substituting (28) into (27) causes the cancellation of the first term (the sum), which yields

$$\boldsymbol{\tau}_n = l \left(\sum_{j=n}^N \mathcal{F}_{aj} - \mathcal{F}_{\text{in}} \right). \quad (29)$$

2) *External Concentrated Load*: The second term on the right-end side of (25) represents the generalized external concentrated load, which, in (26), is referred to as

$$\mathbf{F}(\mathbf{q}) = [\mathbf{F}_1^T \mathbf{F}_2^T \cdots \mathbf{F}_N^T]^T \in \mathbb{R}^{6N}$$

where each element is simply

$$\mathbf{F}_n = \mathbf{S}_n^T(\bar{X})\mathcal{F}_p. \quad (30)$$

3) *Inertial, Drag, and Gravitational Matrices*: Let us now break down each matrix coefficient of the dynamic equation

(26). Looking at (25), the generalized inertia matrix $\mathbf{M}(\mathbf{q}) \in \mathbb{R}^{6N \times 6N}$ is a symmetric, positive define matrix and its 6×6 block element of block row n , and block column m is calculated as follows:

$$\mathbf{M}_{(n,m)} = \sum_{i=\max(n,m)}^N \int_{L_{i-1}}^{L_i} \mathbf{S}_n^T \mathbf{M}_a \mathbf{S}_m \, dX \quad (31)$$

where we have exploited the fact that for $i < \max(n, m)$ or equivalently $X < L_{\max(n,m)-1}$ either $\mathbf{S}_n(X)$ or $\mathbf{S}_m(X)$ is equal to $\mathbf{0}_{6 \times 6}$ (see Fig. 3). Similarly, for the Coriolis matrices $\mathbf{C}_1(\mathbf{q}, \dot{\mathbf{q}}), \mathbf{C}_2(\mathbf{q}, \ddot{\mathbf{q}}) \in \mathbb{R}^{6N \times 6N}$ we obtain

$$\mathbf{C}_{1(n,m)} = \sum_{i=\max(n,m)}^N \int_{L_{i-1}}^{L_i} \mathbf{S}_n^T \text{ad}_{\mathbf{J}\dot{\mathbf{q}}}^* \mathbf{M}_a \mathbf{S}_m \, dX \quad (32)$$

$$\mathbf{C}_{2(n,m)} = \sum_{i=\max(n,m)}^N - \int_{L_{i-1}}^{L_i} \mathbf{S}_n^T \mathbf{M}_a \text{ad}_{\sum_{j=m+1}^i \mathbf{S}_j \dot{\mathbf{q}}} \mathbf{S}_m \, dX \quad (33)$$

while, for the drag matrix $\mathbf{D}(\mathbf{q}, \dot{\mathbf{q}}) \in \mathbb{R}^{6N \times 6N}$, we get

$$\mathbf{D}_{(n,m)} = \sum_{i=\max(n,m)}^N \int_{L_{i-1}}^{L_i} \mathbf{S}_n^T \mathbf{D} \mathbf{S}_m |\mathbf{J}\dot{\mathbf{q}}|_v \, dX. \quad (34)$$

With the same reasoning, the block element of block row n of the gravitational-buoyancy matrix $\mathbf{N}(\mathbf{q}) \in \mathbb{R}^{6N \times 6}$ is as follows:

$$\mathbf{N}_{(n)} = (1 - \rho_w/\rho) \sum_{i=n}^N \int_{L_{i-1}}^{L_i} \mathbf{S}_n^T \mathbf{M} \text{Ad}_{\mathbf{g}}^{-1} \, dX. \quad (35)$$

We now have all the ingredients to process the joint dynamics (26) and reconstruct the shape, velocity, and acceleration of the soft manipulator with (8), (19), and (21).

IV. RECURSIVE ALGORITHMS

In this section, the dynamic equation obtained above is solved by extending to soft manipulators, the composite-rigid-body and articulated-body algorithms of rigid robotics [30]. The first one aims to efficiently calculate the coefficient matrices of (26), while the second one is a Newton–Euler (N–E) algorithm that concentrates on the inertia and external forces of a set of sections on a parent section called handle [30]. The performances of the two algorithms are compared through a cantilever beam

$$\begin{aligned}
 M, C_1, D: & \quad \boxed{\text{dark gray}} = \boxed{\text{white}} + \boxed{\text{white}} + \boxed{\text{dark gray}} + \boxed{\text{dark gray}} \\
 N: & \quad \boxed{\text{dark gray}} = \boxed{\text{white}} + \boxed{\text{white}} + \boxed{\text{dark gray}} + \boxed{\text{white}} \\
 C_2: & \quad \boxed{\text{dark gray}} = \boxed{\text{white}} + \boxed{\text{white}} + \boxed{\text{dark gray}} + \boxed{\text{white}}
 \end{aligned}$$

Fig. 4. Composition of the coefficient matrices from the contribution of the nonzero block matrices due to each section (e.g., four sections).

simulation against an upwind finite difference solution of the continuous Cosserat model (4).

This example will also allow us to show how the PCS model copes with nonconstant internal loads.

A. Composite-Body Algorithm

The basic idea of the composite-body algorithm (where we have removed the word rigid to stress the proposed extension to soft manipulators) is that each section of the soft manipulator contributes to a very specific set of block elements of the coefficient matrices. In particular, the nonzero block elements due to section n of the mass matrix M , the first Coriolis matrix C_1 , and the drag matrix D are those located in the square block matrix of block rows $1 - n$ and block column $1 - n$, while for the gravitational matrix N , they compose the block rows from 1 to n of the only block column and finally, for the second Coriolis matrix C_2 , the nonzero block elements form a rectangular block matrix of block rows $1 - n$ and block column $1 - n - 1$ (see Fig. 4). This can be seen by splitting the integrals in the coefficient matrices of (25) into the N integrals corresponding to each section, then the nonzero square block-matrix rise from the varying structure of the Jacobian $J(X)$ (and $\dot{J}(X)$ for C_2) with respect to X as shown in Fig. 3.

An efficient way to implement this technique, is to benefit from the results of the calculations given by the previous section. Going further into details, at a certain $L_{n-1} < X \leq L_n$, the Jacobian element $S_{n-1}(X)$ has only one member which actually depends on X , all the rest can be inherited from the last evaluation of the same quantity in the previous section ($S_{n-1}(L_{n-1})$), as it can be visualized by inspecting (20). This is used in the calculation of $J(X)$ and the adjoint elements of C_2 (after multiplication with ξ_{n-1}). Furthermore, $\eta(L_{n-1})$ and $g(L_{n-1})$ are calculated respectively through (13) and (10) to obtain the coadjoint member in C_1 and the adjoint member in N .

B. Articulated-Body Algorithm

The articulated-body algorithm is divided into three steps, or better, three passes.

1) *First Pass:* In the first pass, (10) and (13) are used to recursively compute, respectively, the configuration $g(X)$ and velocity $\eta(X)$ of each cross-section X of the manipulator from the base to the tip.

2) *Second Pass:* The core of the algorithm lies on the articulated-body inertia $\mathcal{M}_n^A \in \mathbb{R}^{6 \times 6}$ and force $\mathcal{P}_n^A \in \mathbb{R}^6$, which allow to group the dynamics of a subsystem starting

at section n into a single equation. The objective of the second pass is to calculate those articulated-body inertia and force for all the sections of the manipulator.

To do so, we project the dynamic equation (4) onto the frame at $X = L_{n-1}$ with $\text{Ad}_{g_n}^*(X)$ and onto the joint space with $S_n^T(X)$ and integrate along the interval $[L_{n-1}, L_n]$. Then, introducing (17), we obtain, respectively

$$\begin{aligned}
 \mathcal{F}_{J_n} = & \mathcal{M}_n^t \dot{\eta}(L_{n-1}) + \mathcal{P}_n^t + \text{Ad}_{g_n}^*(L_n) \mathcal{F}_{J_{n+1}} \\
 & + \int_{L_{n-1}}^{L_n} \text{Ad}_{g_n}^* \mathcal{M} \left(S_n \ddot{\xi}_n + \text{ad}_x \eta(L_{n-1}) S_n \dot{\xi}_n \right) dX \quad (36)
 \end{aligned}$$

and

$$\begin{aligned}
 \left(\int_{L_{n-1}}^{L_n} S_n^T \mathcal{M} S_n dX \right) \ddot{\xi}_n = & \underline{\tau}_n - S_n^T(L_n) \mathcal{F}_{J_{n+1}} \\
 - \int_{L_{n-1}}^{L_n} S_n^T \mathcal{M} \left({}^x \dot{\eta}(L_{n-1}) + \text{ad}_x \eta(L_{n-1}) S_n \dot{\xi}_n \right) dX \\
 - \int_{L_{n-1}}^{L_n} S_n^T (\text{ad}_\eta^* \mathcal{M} \eta - \bar{\mathcal{F}}_e) dX \quad (37)
 \end{aligned}$$

where $\mathcal{F}_{J_n}, \mathcal{F}_{J_{n+1}} \in \mathbb{R}^6$ are the force transmitted across the cross-section at $X = L_{n-1}$ and $X = L_n$ respectively, $\mathcal{M}_n^t \in \mathbb{R}^{6 \times 6}$, $\mathcal{P}_n^t \in \mathbb{R}^6$ are the total mass and total force of section n (see Appendix A-1) and ${}^x \eta(L_{n-1}) = \text{Ad}_{g_n}^{-1} \eta(L_{n-1})$ [similarly for ${}^x \dot{\eta}_i(L_{n-1})$].

Now, imagine to know \mathcal{M}_{n+1}^A and \mathcal{P}_{n+1}^A for a subsequent section $n+1$, then we have:

$$\mathcal{F}_{J_{n+1}} = \mathcal{M}_{n+1}^A \dot{\eta}(L_n) + \mathcal{P}_{n+1}^A \quad (38)$$

whose right-hand side can be substituted into (37), which yields

$$\begin{aligned}
 \left[\int_{L_{n-1}}^{L_n} S_n^T \mathcal{M} S_n dX + (S_n^T \mathcal{M} \mathcal{M}_{n+1}^A S_i) (L_n) \right] \ddot{\xi}_n = & \tau_n \\
 - \left[\int_{L_{n-1}}^{L_n} S_n^T \mathcal{M} \text{Ad}_{g_n}^{-1} dX + (S_n^T \mathcal{M}_{n+1}^A \text{Ad}_{g_n}^{-1}) (L_n) \right] \dot{\eta}(L_{n-1}) \\
 - \left[\int_{L_{n-1}}^{L_n} S_n^T \mathcal{M} \text{ad}_x \eta(L_{n-1}) S_n dX + (S_n^T \mathcal{M}_{n+1}^A \text{ad}_x \eta(L_{n-1}) S_n) \right. \\
 \left. (L_n) \right] \dot{\xi}_n - \left[\int_{L_{n-1}}^{L_n} S_n^T (\text{ad}_\eta^* \mathcal{M} \eta - \bar{\mathcal{F}}_e) dX + S_n^T(L_n) \mathcal{P}_{n+1}^A \right] \quad (39)
 \end{aligned}$$

where (17) has been used to represents $\dot{\eta}(L_n)$.

Finally, solving (39) for $\ddot{\xi}_n$ and introducing the result, together with the right-hand side of (38) into (36) produces an equation of the form

$$\mathcal{F}_{J_n} = \mathcal{M}_n^A \dot{\eta}(L_{n-1}) + \mathcal{P}_n^A \quad (40)$$

which gives the values of the articulated-body inertia \mathcal{M}_n^A and force \mathcal{P}_n^A for a section n , given their values at the subsequent section $n+1$ (see Appendix A-2 for the explicit formula).

By recursively applying this result from the tip of the manipulator (where the values of \mathcal{M}_{n+1}^A and \mathcal{P}_{n+1}^A are zero) to the base, allows to obtain the articulated-body inertia and force for all the sections of the manipulator.

3) *Third Pass:* In the third pass, (17) and (39) are used to recursively compute $\dot{\xi}_n$ and $\dot{\eta}(X)$ from the base of the manipulator to the tip.

C. Cantilever Beam Comparison

Even if one could manage to design the actuation of a soft manipulator in order to have constant internal load in each section, nonconstant internal loads due to gravity, external forces, and inertial forces are unavoidable in realistic condition. For this reason, it is important to know how the discrete Cosserat model handles a force causing nonconstant internal load and what the effects are, in terms of accuracy, of the result.

In order to test the model with a nonconstant internal load scenario and compare the performances of the two recursive algorithms, the continuous Cosserat model (4) and the discrete Cosserat model (26) are applied in the following to a cantilever beam with vertical tip load. The simulated beam is of cylindrical shape, with length $L = 250$ mm, radius equal to 10 mm, Young modulus $E = 110$ kPa, shear viscosity modulus $v = 0.3$ kPa·s, Poisson modulus equal to 0 and mass density $\rho = 2000$ kg/m³. The beam lies on the right side of the spatial frame (see Fig. 2) and shares the Z axis with this frame. Therefore, the map between the spatial frame and the base frame is

$$\mathbf{g}_r = \begin{pmatrix} 0 & -1 & 0 & 0 \\ 1 & 0 & 0 & 0 \\ 0 & 0 & 1 & 0 \\ 0 & 0 & 0 & 1 \end{pmatrix}.$$

Finally, the external tip load points in the positive Y direction with respect to the fixed base frame and is applied at $\bar{X} = L$, thus it has the form

$$\mathcal{F}_p = \begin{pmatrix} \mathbf{R}^T(L) & \mathbf{0}_{3 \times 3} \\ \mathbf{0}_{3 \times 3} & \mathbf{R}^T(L) \end{pmatrix} \begin{pmatrix} 0 \\ 0 \\ 0 \\ 0 \\ 10 \\ 0 \end{pmatrix}$$

with unit reference of 10^{-3} N. The tip load linearly increases from zero to its maximum value in 1 s and then maintains a constant value for the rest of the simulation time.

The continuous and discrete model were numerically solved in MATLAB. For the continuous model, the numerical scheme used is a decentralized space differentiation (upwind) finite-difference method, based on a Dormand–Prince time integration method with local extrapolation (by means of the MATLAB `ode45` function) [17]. A spatial distribution of one material point for every 5 mm was adopted. For the discrete model, the same Dormand–Prince time integration method and the same spatial distribution of material points were used. Both the composite-body and the articulated-body algorithms have been tested for a range of up to ten sections.

1) *Accuracy Comparison:* Fig. 5 (top) shows the resulting curvature of the continuous cantilever as a function of space and time, followed by the curvatures of the first sections of the

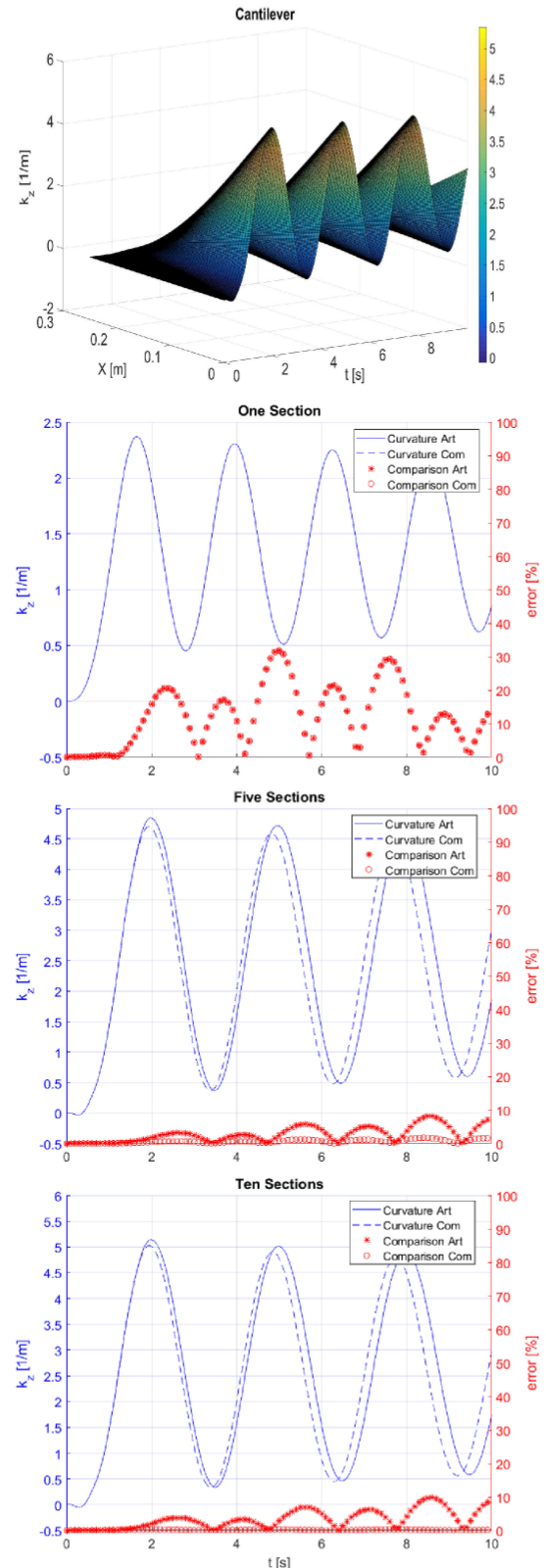


Fig. 5. From top, curvature of the continuous cantilever as a function of space and time, followed by the curvature of the first sections of the discrete cantilever divided into, respectively, one, five, and ten sections (blue lines), for both the algorithms. The Euclidean tip position error expressed as percentage of the total length L is also indicated with red markers.

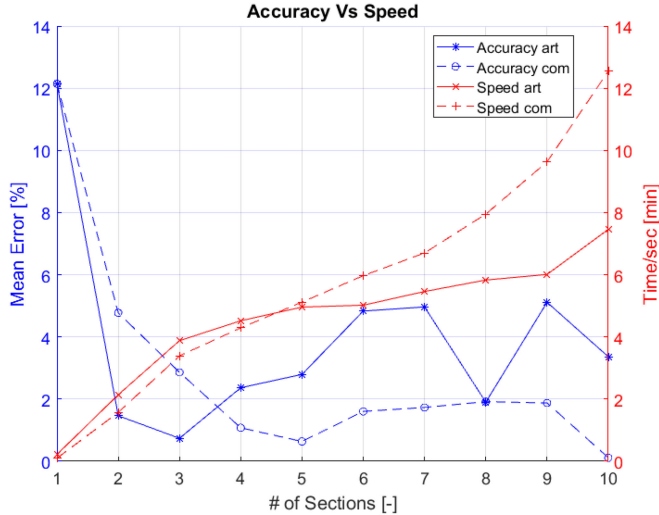


Fig. 6. Accuracy and computational time performances of the composite-body (dashed line) and articulated-body (solid line) algorithms against the number of discrete sections.

discrete cantilever divided into, respectively, one, five, and ten sections, for both the articulated-body (solid blue lines) and the composite-body (dashed blue lines) algorithms.

We immediately notice that the oscillation frequency for the one section case is much higher than that of the continuous cantilever for both the algorithms. This discrepancy is quantified at each time by the Euclidean tip position error expressed in percentage of the total length L (red asterisks and red circles, respectively, for the articulated-body and composite-body algorithms). Intuitively, this can be explained by the fact that the additional constraint of constant strains applied to the Cosserat microsolids in the discrete model makes the system more rigid. As expected, the oscillation frequency progressively slows down toward the continuous value with the increase of the number of sections while, accordingly, the error decreases, steadily settling below 5%.

A complete representation of this tendency is given in Fig. 6, where the accuracy (as the time mean of the normalized Euclidean distance of the tips) and speed of the two algorithms are shown against the number of discrete sections. For a more specific evaluation of the PCS model accuracy, we refer the reader to the experimental Section V.

2) *Computational Time Comparison:* For what concerns the computational cost, the continuous model numerically solved with upwind finite-difference scheme required around 19 min of calculation, in order to compute 1 s of simulation, and around 2 42 087 timesteps of about 4.1×10^{-5} s each for a total of 10 s of simulation. As shown in Fig. 6, the discrete Cosserat models demonstrate better performances in terms of computational time per second of simulation with respect to the continuous model, regardless of the algorithm or the number of sections used. This is because the smaller number of state variables of the discrete Cosserat model allows for a much larger average timestep size. As a matter of fact, even with the highest number of sections, both discrete algorithms required only $\sim 24\ 150$ timesteps of about 4.1×10^{-4} s each to complete 10 s of simulation.

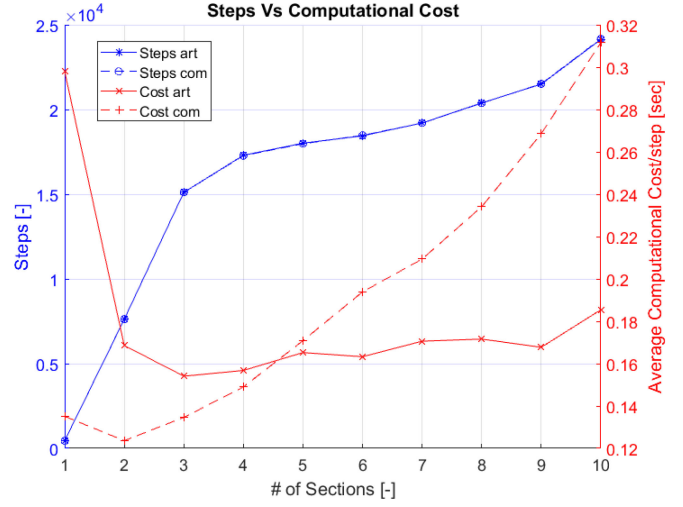


Fig. 7. Number of timesteps and timestep average computational cost for the composite-body (dashed line) and articulated-body (solid line) algorithms against the number of discrete sections. Notice that the two algorithms required practically the same number of timesteps to complete 10 s of simulation.

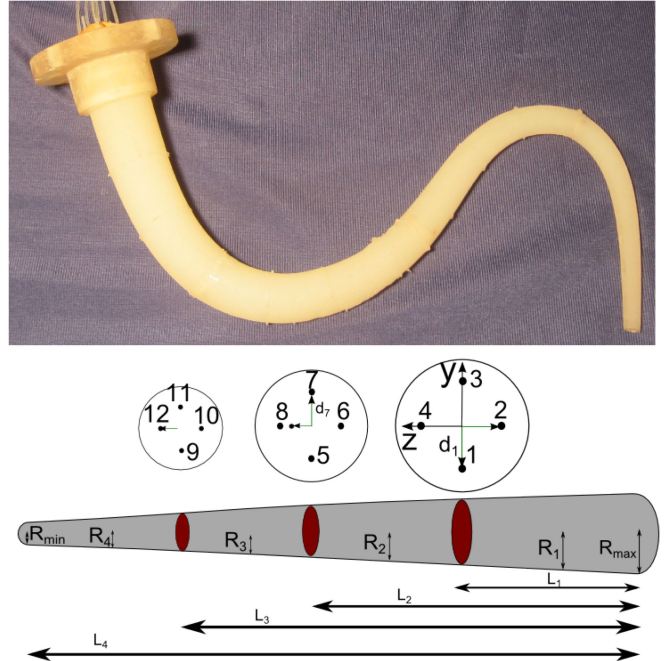


Fig. 8. Real prototype (top) and schematic (bottom) of the soft manipulator used in the experiments.

It is worth to notice that among the two algorithms, the articulated-body algorithm has a higher computational time for a number of sections less than five, but a lower computational time otherwise. This is shown in terms of computational time per second of simulation in Fig. 6 and in terms of timestep's average computational cost in Fig. 7. This trend is in line with the theoretical results reported in [30] about the computational performance of the rigid-body counterparts of those algorithms.

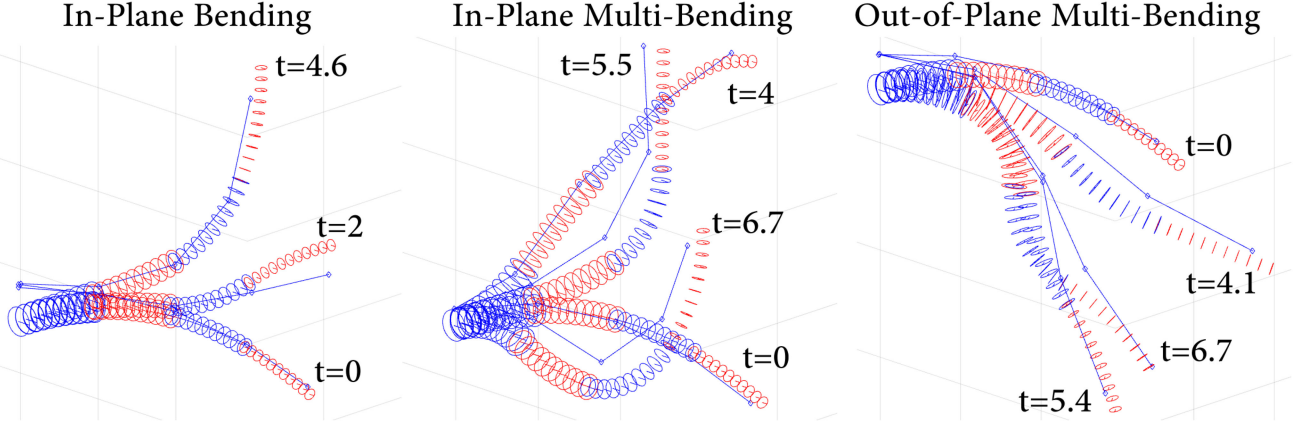


Fig. 9. Several snapshots of the comparison between the real (piecewise linear curve) and PCS-simulated (cross-sections) prototype for the in-plane bending, in-plane multibending, and out-of-plane multibending experiments (see also the multimedia attachment).

V. EXPERIMENTAL RESULTS

In this section, the PCS dynamic model performances are compared against experimental data. In order to evaluate the results with respect to the continuous Cosserat model, we have used the same prototype, parameters, and experimental data provided in [17], to which we refer for more exhaustive details on the experimental platform and measurement setup.

In short, the prototype is composed of a single conical piece of silicone, with a base radius R_{\max} and a tip radius R_{\min} , actuated by 12 cables embedded inside the robot body. The cables run parallel to the midline at a distance d_j ($j \in \{1, 2, \dots, 12\}$) and are anchored four at a time at three different lengths along the robot arm (L_1, L_2, L_3), with a relative angle of 90° (see Fig. 8). During operation, the cable tensions, driven by servomotors, are measured by force sensors while the motion of the arm is recorded with two high-speed cameras. The 3-D motion is then reconstructed through a process based on the direct linear transformation by using visual markers positioned at the tip of each section.

The soft manipulator has been tested for three different conditions, a single bending motion produced by cable 11, an in-plane multibending produced by a sequence of activation of cables 9, 11, 1, and 3, and an out-of-plane multibending produced by cables 11, 5, and 2. The details of the cable activation is reported in Fig. 10 (top three graphs).

In [17], it has been found that in this case, the drag and added mass matrices can be expressed as

$$\mathbf{D} = \begin{pmatrix} \mathbf{0}_{3 \times 3} & \mathbf{0}_{3 \times 3} \\ \mathbf{0}_{3 \times 3} & \mathbf{D} \end{pmatrix}, \quad \mathbf{A} = \begin{pmatrix} \mathbf{0}_{3 \times 3} & \mathbf{0}_{3 \times 3} \\ \mathbf{0}_{3 \times 3} & \mathbf{A} \end{pmatrix}$$

where $\mathbf{D}(X) = \text{diag}(1/2\pi C_x, C_y, C_z)R\rho_w$ and $\mathbf{A}(X) = \text{diag}(0, B_y, B_z)A\rho_w$, $R(X)$ being the radius of the soft arm and C_x, C_y, C_z, B_y, B_z being fluid dynamic coefficients. The mechanical and geometrical parameters of the arm are shown in Table I.

Regarding the numerical aspects, as for the cantilever beam comparison, the numerical scheme used to solve the continuous model is a decentralized space differentiation (upwind) finite difference method, based on a Dormand–Prince time integra-

TABLE I
DESIGN PARAMETERS OF THE PROTOTYPE

Parameter	Value	Parameter	Value
R_{\max}	15 mm	d_1, d_2, d_3, d_4	9 mm
R_{\min}	4 mm	d_5, d_6, d_7, d_8	6 mm
L_1	98 mm	$d_9, d_{10}, d_{11}, d_{12}$	3 mm
L_2	203 mm	gr	$9.81 \frac{m}{s^2}$
L_3	311 mm	ρ_w	$1.02 \frac{kg}{dm^3}$
L_4	418 mm	C_x	0.01
E	110 kPa	C_y	2.5
μ	300 Pa · s	C_z	2.5
ν	0.5	B_y	1.5
ρ	$1.08 \frac{kg}{dm^3}$	B_z	1.5

tion method with local extrapolation [17]. A spatial distribution of one material point for every 10 mm is adopted this time. For the PCS model, the same Dormand–Prince time integration method and the same spatial distribution of material points is used.

A. Comparison

In order to exploit the dynamic equations developed in Section III-B, the soft manipulator has been modeled as a stack of four cylindrical constant strain sections defined by L_1, L_2, L_3, L_4 , with a radius equal to the mean of the prototype radius for each section (R_1, R_2, R_3 , and R_4 in Fig. 8). Due to its better computational performances observed in the previous section, the dynamics and kinematic equations of the PCS model have been solved by implementing the articulated-body algorithm of Section IV-B for the three load conditions of the experiments described above (in-plane bending, in-plane multibending, and out-of-plane multibending). Several snapshots of the reconstructed real and simulated (with the articulated-body algorithm) pose are shown in Fig. 9 (see also the multimedia attachment). To better appreciate the torsional effect due to the external and actuation loads in the out-of-plane multibending motion, Fig. 11 reports the time plot of the torsion of each

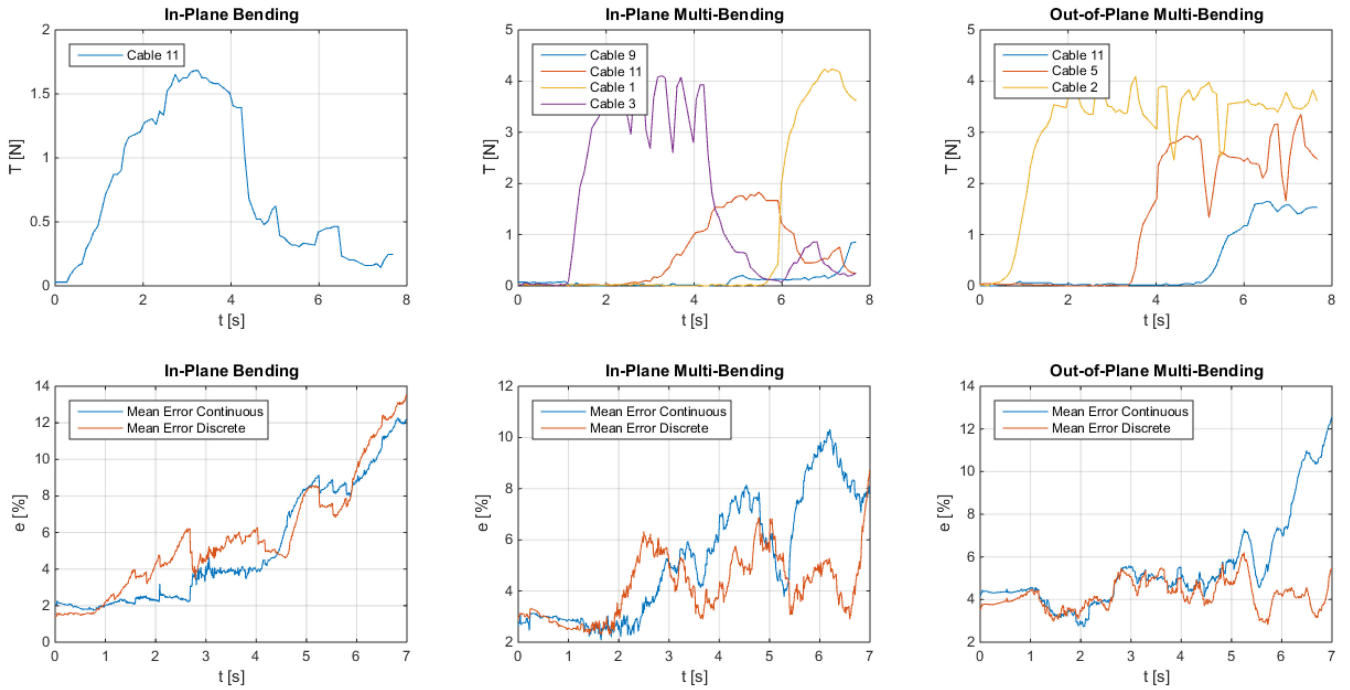


Fig. 10. Measured cable tensions which represent the input of the model (top) and experimental results (bottom) with a comparison between the results of the continuous Cosserat model of [17] and the present discrete Cosserat model.

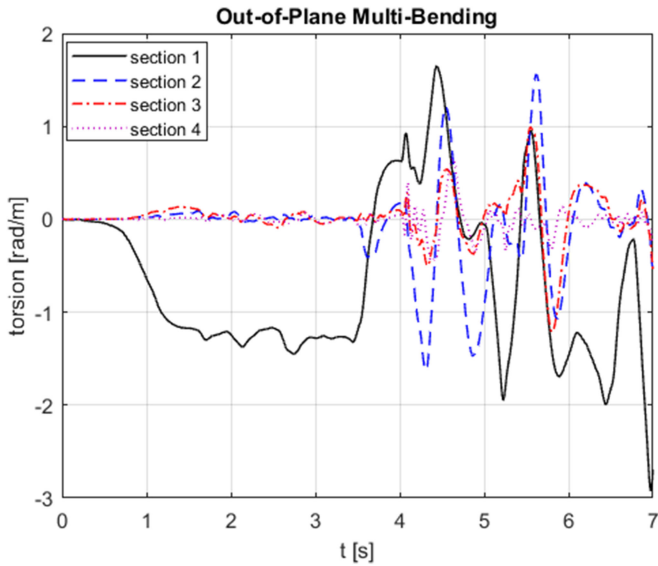


Fig. 11. Time plot of the torsion of each of the four robot arm sections for the out-of-plane multibending motion.

of the four robot arm sections. This effect, which cannot be captured with a constant curvature approach, adds up to a tip torsional rotation of around 20° at particular instants of time, disruptively changing the shape of the robot arm by pairing with the curvatures in the cross-section plane directions. The error is calculated as the normalized mean at each timestep of the Euclidean distances between the simulated ($\mathbf{u}(X, t)$) and real ($\mathbf{u}_r(X, t)$) tip position of each section, as shown in (41). The results of the tests are reported in Fig. 10, together with the one

obtained in [17] with the continuous Cosserat model

$$e(t) = \frac{\sum_{i=1}^4 \|\mathbf{u}(L_i, t) - \mathbf{u}_r(L_i, t)\|}{4L_4}. \quad (41)$$

As observed in Section IV-C2, the discrete Cosserat model performs better in terms of computational cost with respect to the upwind finite-difference solution of the continuous Cosserat model. For the actual experimental conditions, the continuous model required a mean of 28 min to compute 1 s of simulation, as reported in [17] (see Section IV-C), while the discrete model required, respectively, 5 min 25 s, 5 min 35 s, and 5 min 30 s for the in-plane bending, in-plane multibending, and out-of-plane multibending cases. On average, this is the 19.5% of the continuous model computational time.

B. Discussion

As can be observed from Fig. 10, the results of the presented discrete model are comparable or even better than the ones obtained with the continuous model. As a matter of fact, the average error in the three cases are respectively 5.1%, 5.2%, and 5.4% for the upwind finite difference solution of the continuous model versus 5.8%, 4.2%, and 4.3% for the PCS model.

In order to further improve the accuracy of the PCS model, an ad hoc calibration of the discrete model parameters may be conducted. Furthermore, the friction of the cables could be included, which in turn, models the hysteresis behavior of the load–unload cycle. As it is highlighted in [17], the hysteresis behavior is clear from the plane-bending experiments, where the error increases drastically after the relaxation of the cable, which is when the load is mainly driven by the friction of the cable against the silicone body. From a geometric point of view,

the number of discrete sections could be increased in order to capture nonnegligible variation of the strain due to external loads. Furthermore, the model could be able to better take into account the variation with respect to X of the mass $\mathcal{M}(X)$ in the calculus of the mass matrix \mathbf{M} as well as the variation of the stiffness and viscosity matrices $\Sigma(X)$, $\Upsilon(X)$ in the calculus of the internal elastic load of τ , which are due to the conical shape of the manipulator.

VI. CONCLUSION AND FUTURE WORK

In conclusion, a new PCS model for multisection soft manipulator dynamics has been presented. The model is based on a discretization of the continuous Cosserat model and therefore inherits fruitful geometrical and mechanical properties from it. Two efficient recursive algorithms have been developed for the PCS model, which extend to soft robotics, the composite-rigid-body and the articulated-body algorithms of rigid robotics [30]. The algorithms' performances have been compared for the benchmark case of a cantilever beam. The PCS model has also been corroborated experimentally for in-plane and out-of-plane multibending motions. The results have been compared with an upwind finite-difference solution of the continuous Cosserat model showing comparable or even better results, in terms of accuracy, and tremendous improvements in terms of computational time.

Finally, this work paves the way to bridge the gap between the usual models of rigid robotics arms and their soft robotics counterparts, thanks to its intrinsic parameterization and general SE(3) geometry. The parameterization used in this paper, based on discrete strain fields, is, in fact, the continuous counterpart of the joint variables parameterization of multibody robotics arms. However, the general strain kinematics of the article, which include extension and shear strains, can be considered as not enough constrained regarding the usual applications in soft robotics. In this respect, it is worth noting that these kinematics can be easily reduced by removing any of the scalar strain field. In other words, by replacing ξ_n and τ_n with

$$\begin{aligned}\boldsymbol{\xi}_n &= \mathbf{B}_n \mathbf{q}_n \\ \boldsymbol{\tau}_n &= \mathbf{B}_n^T l \left(\sum_{j=n}^N \mathcal{F}_{aj} - \mathcal{F}_{in} \right)\end{aligned}$$

where \mathbf{B}_n is a basis of the subspace of $\mathfrak{se}(3)$ relative to the particular kinematics. One can then restart the integration of the article and obtain the same results in these particular simplified cases. This extension is part of the contribution recently accepted to 2018 IEEE International Conference on Robotics and Automation [44].

APPENDIX A FORMULAS

In the following, explicit formulas for the components of the recursive articulated-body algorithm are given.

1) *Total Mass and Force:* For a section n , we have

$$\mathcal{M}_n^t = \int_{L_{n-1}}^{L_n} \text{Ad}_{\mathbf{g}_n}^* \mathcal{M} \text{Ad}_{\mathbf{g}_n}^{-1} dX \quad (42)$$

$$\mathcal{P}_n^t = \int_{L_{n-1}}^{L_n} \text{Ad}_{\mathbf{g}_n}^* (\text{ad}_{\boldsymbol{\eta}}^* \mathcal{M} \boldsymbol{\eta} - \bar{\mathcal{F}}_e) dX. \quad (43)$$

2) *Articulated-Body Inertia and Force:* For a section n with a subsequent section $n+1$, we have

$$\begin{aligned}\mathcal{M}_n^A &= \mathcal{M}_n^t + (\text{Ad}_{\mathbf{g}_n}^* \mathcal{M}_{n+1}^A \text{Ad}_{\mathbf{g}_n}^{-1}) (L_n) \\ &\quad - \left[\int_{L_{n-1}}^{L_n} \text{Ad}_{\mathbf{g}_n}^* \mathcal{M} \mathbf{S}_n dX + (\text{Ad}_{\mathbf{g}_n}^* \mathcal{M}_{n+1}^A \mathbf{S}_n) (L_n) \right] \\ &\quad \left[\int_{L_{n-1}}^{L_n} \mathbf{S}_n^T \mathcal{M} \mathbf{S}_n dX + (\mathbf{S}_n^T \mathcal{M}_{n+1}^A \mathbf{S}_n) (L_n) \right]^{-1} \\ &\quad \left[\int_{L_{n-1}}^{L_n} \mathbf{S}_n^T \mathcal{M} \text{Ad}_{\mathbf{g}_n}^{-1} dX + (\mathbf{S}_n^T \mathcal{M}_{n+1}^A \text{Ad}_{\mathbf{g}_n}^{-1}) (L_n) \right] \quad (44) \\ \mathcal{P}_n^A &= \mathcal{P}_n^t + \text{Ad}_{\mathbf{g}_n}^*(L_n) \mathcal{P}_{n+1}^A + \left[\int_{L_{n-1}}^{L_n} \text{Ad}_{\mathbf{g}_n}^* \mathcal{M} \text{Ad}_{\boldsymbol{\eta}(L_{n-1})} \mathbf{S}_n dX \right. \\ &\quad \left. + (\text{Ad}_{\mathbf{g}_n}^* \mathcal{M}_{n+1}^A \text{ad}_{\boldsymbol{\eta}(L_{n-1})} \mathbf{S}_n) (L_n) \right] \dot{\boldsymbol{\xi}}_n + \\ &\quad \left[\int_{L_{n-1}}^{L_n} \text{Ad}_{\mathbf{g}_n}^* \mathcal{M} \mathbf{S}_n dX + (\text{Ad}_{\mathbf{g}_n}^* \mathcal{M}_{n+1}^A \mathbf{S}_n) (L_n) \right] \\ &\quad \left[\int_{L_{n-1}}^{L_n} \mathbf{S}_n^T \mathcal{M} \mathbf{S}_n dX + (\mathbf{S}_n^T \mathcal{M}_{n+1}^A \mathbf{S}_n) (L_n) \right]^{-1} \left\{ \boldsymbol{\tau}_n \right. \\ &\quad \left. - \left[\int_{L_{n-1}}^{L_n} \mathbf{S}_n^T \mathcal{M} \text{Ad}_{\boldsymbol{\eta}(L_{n-1})} \mathbf{S}_n dX + (\mathbf{S}_n^T \mathcal{M}_{n+1}^A \text{ad}_{\boldsymbol{\eta}(L_{n-1})} \mathbf{S}_n) \right. \right. \\ &\quad \left. \left. (L_n) \right] \dot{\boldsymbol{\xi}}_n - \left[\int_{L_{n-1}}^{L_n} \mathbf{S}_n^T (\text{ad}_{\boldsymbol{\eta}}^* \mathcal{M} \boldsymbol{\eta} - \bar{\mathcal{F}}_e) dX + \mathbf{S}_n^T (L_n) \mathcal{P}_{n+1}^A \right] \right\}. \quad (45)\end{aligned}$$

REFERENCES

- [1] D. Rus and M. T. Tolley, "Design, fabrication and control of soft robots," *Nature*, vol. 521, no. 7553, pp. 467–475, May 2015.
- [2] S. Kim, C. Laschi, and B. Trimmer, "Soft robotics: A bioinspired evolution in robotics," *Trends Biotechnol.*, vol. 31, no. 5, pp. 287–294, 2013.
- [3] K. Suzumori, S. Iikura, and H. Tanaka, "Development of flexible microactuator and its applications to robotic mechanisms," in *Proc. IEEE Int. Conf. Robot. Autom.*, 1991, vol. 2, pp. 1622–1627.
- [4] K. Suzumori, "Elastic materials producing compliant robots," *Robot. Auton. Syst.*, vol. 18, no. 1, pp. 135–140, 1996.
- [5] C. Laschi, B. Mazzolai, and M. Cianchetti, "Soft robotics: Technologies and systems pushing the boundaries of robot abilities," *Sci. Robot.*, vol. 1, no. 1, 2016, doi: [10.1126/scirobotics.aah3690](https://doi.org/10.1126/scirobotics.aah3690).
- [6] R. Kang, D. T. Branson, E. Guglielmino, and D. G. Caldwell, "Dynamic modeling and control of an octopus inspired multiple continuum arm robot," *Comput. Math. Appl.*, vol. 64, no. 5, pp. 1004–1016, 2012.
- [7] R. J. Webster and B. A. Jones, "Design and kinematic modeling of constant curvature continuum robots: A review," *Int. J. Robot. Res.*, vol. 29, no. 13, pp. 1661–1683, 2010.
- [8] B. A. Jones and I. D. Walker, "Kinematics for multisection continuum robots," *IEEE Trans. Robot.*, vol. 22, no. 1, pp. 43–55, Feb. 2006.

- [9] I. S. Godage, G. A. Medrano-Cerda, D. T. Branson, E. Guglielmino, and D. G. Caldwell, "Dynamics for variable length multisection continuum arms," *Int. J. Robot. Res.*, vol. 35, pp. 695–722, 2015.
- [10] V. Falkenhahn, T. Mahl, A. Hildebrandt, R. Neumann, and O. Sawodny, "Dynamic modeling of bellows-actuated continuum robots using the Euler-lagrange formalism," *IEEE Trans. Robot.*, vol. 31, no. 6, pp. 1483–1496, Dec. 2015.
- [11] S. Antman, *Nonlinear Problems of Elasticity*, Applied Mathematical Sciences. New York, NY, USA: Springer, 2006.
- [12] G. S. Chirikjian, "A continuum approach to hyper-redundant manipulator dynamics," in *Proc. IEEE/RSJ Int. Conf. Intell. Robots Syst.*, vol. 2, 1993, pp. 1059–1066.
- [13] F. Boyer, M. Porez, and W. Khalil, "Macro-continuous computed torque algorithm for a three-dimensional eel-like robot," *IEEE Trans. Robot.*, vol. 22, no. 4, pp. 763–775, Aug. 2006.
- [14] F. Boyer and M. Porez, "Multibody system dynamics for bio-inspired locomotion: From geometric structures to computational aspects," *Bioinspiration Biomimetics*, vol. 10, no. 2, 2015, Art. no. 025007.
- [15] D. C. Rucker and R. J. Webster, "Statics and dynamics of continuum robots with general tendon routing and external loading," *IEEE Trans. Robot.*, vol. 27, no. 6, pp. 1033–1044, Dec. 2011.
- [16] F. Renda, M. Cianchetti, M. Giorelli, A. Arienti, and C. Laschi, "A 3d steady-state model of a tendon-driven continuum soft manipulator inspired by the octopus arm," *Bioinspiration Biomimetics*, vol. 7, no. 2, 2012, Art. no. 025006.
- [17] F. Renda, M. Giorelli, M. Calisti, M. Cianchetti, and C. Laschi, "Dynamic model of a multibending soft robot arm driven by cables," *IEEE Trans. Robot.*, vol. 30, no. 5, pp. 1109–1122, Oct. 2014.
- [18] I. Tunay, "Spatial continuum models of rods undergoing large deformation and inflation," *IEEE Trans. Robot.*, vol. 29, no. 2, pp. 297–307, Apr. 2013.
- [19] F. Renda, F. Giorgio-Serchi, F. Boyer, and C. Laschi, "Modelling cephalopod-inspired pulsed-jet locomotion for underwater soft robots," *Bioinspiration Biomimetics*, vol. 10, no. 5, pp. 1–12, 2015.
- [20] F. Renda, F. Giorgio-Serchi, F. Boyer, C. Laschi, J. Dias, and L. Seneviratne, "A unified multi-soft-body dynamic model for underwater soft robots," *Int. J. Robot. Res.*, vol. 37, no. 6, pp. 648–666, 2018.
- [21] F. Largilliere, V. Verona, E. Coevoet, M. Sanz-Lopez, J. Dequidt, and C. Duriez, "Real-time control of soft-robots using asynchronous finite element modeling," in *Proc. IEEE Int. Conf. Robot. Autom.*, 2015, pp. 2550–2555.
- [22] J. C. Simo and L. Vu-Quoc, "On the dynamics in space of rods undergoing large motions a geometrically exact approach," *Comput. Methods Appl. Mech. Eng.*, vol. 66, no. 2, pp. 125–161, 1988.
- [23] V. Sonnevile, A. Cardona, and O. Brüls, "Geometrically exact beam finite element formulated on the special Euclidean group SE(3)," *Comput. Methods Appl. Mech. Eng.*, vol. 268, pp. 451–474, 2014.
- [24] G. Jelenić and M. A. Crisfield, "Geometrically exact 3d beam theory: Implementation of a strain-invariant finite element for statics and dynamics," *Comput. Methods Appl. Mech. Eng.*, vol. 171, no. 1, pp. 141–171, 1999.
- [25] F. Boyer, G. De Nayer, A. Leroyer, and M. Visonneau, "Geometrically exact Kirchhoff beam theory: Application to cable dynamics," *J. Comput. Nonlinear Dyn.*, vol. 6, no. 4, pp. 041004–041014, 2011.
- [26] P. Jung, S. Leyendecker, J. Linn, and M. Ortiz, "A discrete mechanics approach to the Cosserat rod theory—1: Static equilibria," *Int. J. Numer. Methods Eng.*, vol. 85, no. 1, pp. 31–60, 2011.
- [27] M. Bergou, M. Wardetzky, S. Robinson, B. Audoly, and E. Grinpun, "Discrete elastic rods," in *ACM Trans. Graph.*, vol. 63, pp. 1–63, 2008.
- [28] J. Spillmann and M. Teschner, "Corde: Cosserat rod elements for the dynamic simulation of one-dimensional elastic objects," in *Eurographics/SIGGRAPH Symposium on Computer Animation*, D. Metaxas and J. Popovic, Eds., Geneva, Switzerland: Eurographics, 2007.
- [29] F. Bertails, "Linear time super-helices," *Comput. Graph. Forum*, New York, USA, vol. 28, no. 2, pp. 417–426, 2009.
- [30] R. Featherstone, *Rigid Body Dynamics Algorithms*, New York, USA: Springer 2008.
- [31] R. M. Murray, Z. Li, and S. S. Sastry, *A Mathematical Introduction to Robotic Manipulation*, Boca Raton, USA: T&F, 1994.
- [32] F. Renda, V. Cacuccio, J. Dias, and L. Seneviratne, "Discrete Cosserat approach for soft robot dynamics: A new piece-wise constant strain model with torsion and shears," in *Proc. IEEE/RSJ Int. Conf. Intell. Robots Syst.*, 2016, pp. 5495–5502.
- [33] F. Renda, M. Cianchetti, H. Abidi, J. Dias, and L. Seneviratne, "Screw-based modeling of soft manipulators with tendon and fluidic actuation," *J. Mech. Robot.*, vol. 9, pp. 041012–041012–8, 2017, doi: 10.1115/1.4036579.
- [34] F. Boyer and F. Renda, "Poincaré's equations for Cosserat media: Application to shells," *J. Nonlinear Sci.*, vol. 27, pp. 1–44, 2016.
- [35] H. Poincaré, "Sur une forme nouvelle des équations de la mécanique," *Compte Rendu de l'Academie des Sci. de Paris*, vol. 132, pp. 369–371, 1901.
- [36] M. Calisti *et al.*, "Study and fabrication of bioinspired octopus arm mockups tested on a multipurpose platform," in *Proc. 3rd IEEE RAS EMBS Int. Conf. Biomed. Robot. Biomechatronics*, 2010, pp. 461–466.
- [37] A. Shiva *et al.*, "Tendon-based stiffening for a pneumatically actuated soft manipulator," *IEEE Robot. Autom. Lett.*, vol. 1, no. 2, pp. 632–637, Jul. 2016.
- [38] C. H. Edwards and D. E. Penney, *Differential Equations and Linear Algebra*. Harlow, UK.: Pearson, 2013.
- [39] J. M. Selig, *Geometric Fundamentals of Robotics*, Monographs in Computer Science. New York, NY, USA: Springer, 2007.
- [40] E. Tatlicioğlu, I. D. Walker, and D. M. Dawson, "New dynamic models for planar extensible continuum robot manipulators," in *Proc. IEEE/RSJ Int. Conf. Intell. Robots Syst.*, 2007, pp. 1485–1490.
- [41] W. S. Rone and P. Ben-Tzvi, "Continuum robot dynamics utilizing the principle of virtual power," *IEEE Trans. Robot.*, vol. 30, no. 1, pp. 275–287, Feb. 2014.
- [42] M. Abata and F. Tovena, *Geometria Differenziale: UNITEXT*. Milan, Italy: Springer, 2011.
- [43] F. Boyer, M. Porez, and A. Leroyer, "Poincaré Cosserat equations for the lighthill three-dimensional large amplitude elongated body theory: Application to robotics," *J. Nonlinear Sci.*, vol. 20, no. 1, pp. 47–79, 2010.
- [44] F. Renda and L. Seneviratne, "A geometric and unified approach for modeling soft-rigid multi-body systems with lumped and distributed degrees of freedom," in *Proc. IEEE Int. Conf. Robot. Autom.*, Brisbane, QLD, 2018, pp. 1567–1574.



Federico Renda received the B.Sc. and M.Sc. degrees in biomedical engineering from the University of Pisa, Pisa, Italy, in 2007 and 2009, respectively. He received the Ph.D. degree in biorobotics in 2014 from the BioRobotics Institute of the Scuola Superiore Sant'Anna, Pisa, Italy. In 2013, he joined the IRCyN Lab at the Ecole des Mines de Nantes, Nantes, France, as a visiting Ph.D. student.

He is currently a Postdoctoral Fellow with the Khalifa University Robotics Institute, Khalifa University of Science, Technology and Research, Abu Dhabi, UAE. His research activities include the geometrically exact modeling of soft robots and its application in design and control.



Frédéric Boyer was born in France in 1967. He received both the Diploma degree in mechanical engineering and the Master of Research degree in mechanics from the Institut Nationale Polytechnique de Grenoble, Grenoble, France, in 1991, and the Ph.D. degree in robotics from the University of Paris VI, Paris, France, in 1994.

He is currently a Professor with the Department of Automatic Control, Ecole des Mines de Nantes (now IMT Atlantique), Nantes, France, where he works with the Robotics Team, and also with the Institut de Recherche en Communication et Cybernétique de Nantes, Nantes, France. His research interests include structural dynamics, geometric mechanics, and biorobotics.

Dr. Boyer was the recipient of the Monpetit Prize from the Academy of Science of Paris, in 2007, for his work in dynamics.



Jorge Dias received the Ph.D. degree in electrical engineering from the University of Coimbra, Portugal, with a specialization in control and instrumentation, in 1994.

He has been a Professor with the Department of Electrical Engineering and Computers and a Researcher with the Institute of Systems and Robotics (ISR) at the University of Coimbra. He also coordinates the research group for artificial perception for intelligent systems and robotics of Institute of Systems and Robotics from University of Coimbra, Coimbra, Portugal, and the Laboratory of Systems and Automation (<http://las.ipn.pt>) from the Instituto Pedro Nunes (IPN), Coimbra, Portugal, a technology transfer institute with the University of Coimbra. Since July 2011, he has been on leave of absence to setup the Robotics Institute and research activities on robotics at Khalifa University, Abu Dhabi, UAE. His research interests include the area of computer vision and robotics and he has been contributing to the field since 1984. He has authored several international journals, books, and conferences.



Lakmal Seneviratne received the B.Sc. degree in engineering and the Ph.D. degree in mechanical engineering from King's College London, London, U.K., in 1980 and 1986, respectively.

He was a Research Associate with the University College London, London, U.K., and an Engineer with GEC Energy Systems Ltd., prior to joining Kings College London as a Lecturer. He is currently a Professor of mechatronics (Professor Emeritus). His research interests include robotics and automation, with special emphasis on the use of engineering mechanics based algorithms to create intelligent behavior in a variety of mechatronic applications.